

Chapter 4

Multi-scale modelling of dry granular flows

4.1 Introduction

The dynamics of a homogeneous granular flow involve at least three distinct scales: the *microscopic scale*, which is characterised by the contact between grains, the *meso-scale* that represents micro-structural effects such as grain rearrangement, and the *macroscopic scale*, where geometric correlations can be observed (see Figure 4.1). Conventionally, granular flows are modelled as a continuum because they exhibit many collective phenomena. However, on a grain scale, the granular materials exhibit complex solid-like and/or fluid-like behaviour. Recent studies, however, suggest that a continuum law may be unable to capture the effect of inhomogeneities at the grain scale level, such as orientation of force chains, which are micro-structural effects. Discrete element methods (DEM) are capable of simulating these micro-structural effects, however they are computationally expensive. In the present study, a multi-scale approach is adopted, using both DEM and continuum techniques, to better understand the rheology of granular flows and the limitations of continuum models.

4.2 Granular column collapse

The collapse of a granular column on a horizontal surface is a simple case of granular flow, however a proper model that describes the flow dynamics is still lacking. Granular flow is modelled as a frictional dissipation process in continuum mechanics but studies showing the lack of influence of inter-particle friction on the energy dissipation and spreading dynamics is surprising. In the present study, the generalised interpolation material point method (GIMPM),



Figure 4.1 Multi-scale modelling of granular materials

- ¹ a hybrid Eulerian – Lagrangian approach, is implemented with Mohr-Coloumb failure criterion
- ² to describe the continuum behaviour of quasi-two dimensional collapse of granular columns.
- ³ The granular column collapse is also simulated using DEM to understand the micro-mechanics
- ⁴ of the flow.

⁵ The granular column collapse experiment involves filling a cylinder of height H_0 and width
⁶ L_0 with a granular material of mass ‘m’. The granular column is then released *en masse*
⁷ by quickly removing the cylinder, thus allowing the granular material to collapse onto the
⁸ horizontal surface, forming a deposit having a final height H_f and radius L_f . A computational
⁹ study on an equivalent two-dimensional configuration (circular disks) was carried out using
¹⁰ Discrete Element and Continuum (MPM) approaches.

¹¹ Lajeunesse et al. (2004) performed axis-symmetric and plane strain tests on granular
¹² column collapse. Granular materials when released suddenly on a horizontal surface exhibit
¹³ transient flow. The mechanism of flow initiation, spreading dynamics and energy dissipation
¹⁴ are studied. The experimental configuration used by Lajeunesse et al. (2004) is shown in
¹⁵ Figure 4.2. Granular material of mass ‘M’ was poured into a container to form a rectangular
¹⁶ heap of length ‘ L_i ’, height ‘ H_i ’ and thickness ‘ W ’. The internal friction angle and the wall
¹⁷ friction between the wall and the glass beads measured by Lajeunesse et al. (2004) are listed
¹⁸ in Table 4.1. The gate was then quickly removed to release the granular mass that spreads in
¹⁹ the horizontal channel until it comes to rest. The final run-out distance ‘ L_f ’ and the collapsed
²⁰ height ‘ H_f ’ were measured. The run-out distance and collapse height were found to exhibit
²¹ power law relation with the initial aspect ratio ‘ a ’ ($= H_i/L_i$) of the column.

4.2 Granular column collapse

3

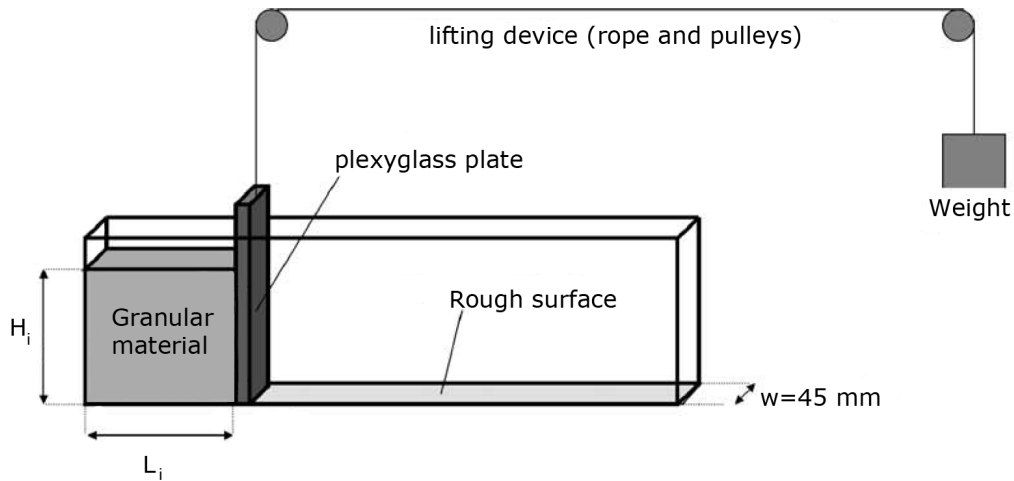


Figure 4.2 Schematic of experimental configuration for 2-D collapse in a rectangular channel, ([Lajeunesse et al., 2004](#))

Table 4.1 Material properties of glass ballotini, ([Lajeunesse et al., 2004](#))

Parameter	Value
Mean diameter	1.15 mm
Repose angle	$22 \pm 0.5^\circ$
Avalanche angle	$27.4 \pm 0.5^\circ$
Wall friction angle	$24.8 \pm 0.2^\circ$

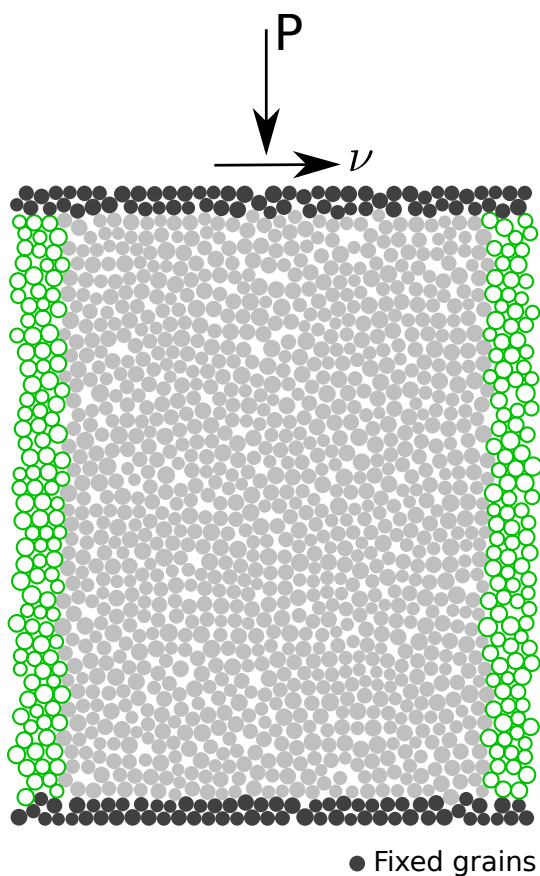


Figure 4.3 Shear test periodic boundary condition

In this study, numerical simulations of the granular column collapse experiments are performed by varying the initial aspect ratio of the column. Discrete Element Method simulations involve modelling the granular column as individual particles. The granular column is prepared by randomly packing poly-disperse grains on a regular lattice and allowing them to undergo free fall due to gravity, forming a randomly packed granular column (see

Krishna Kumar Soundararajan: Add Chapter reference

The grains are allowed to reach a stable equilibrium after undergoing some elastic compressions due to gravity. The overlaps between particles are determined by the stiffness k_n of the spring in the normal direction. Typically, average overlaps in the range 0.1 to 1.0% are desirable and the spring constant is chosen to produce particle overlaps in this range. The stiffness is determined using the following equation:

$$k_n = \frac{2\pi G}{(1-\nu)[2\ln(\frac{2r}{A}) - 1]} \quad (4.1)$$

$$A = \left[\frac{2r(1-\nu)f_n}{\pi G} \right]^{\frac{1}{2}} \quad (4.2)$$

where f_n is the normal contact force; G is the shear modulus; ν is the Poisson's ratio and r is the radius of the grain. A simpler form of stiffness for a spherical grain is defined as:

$$k_n = 4ER \quad (4.3)$$

where E is the Young's modulus of the material and R is the radius of the grain. The normal damping coefficient C_n is chosen to give a required coefficient of restitution ε (defined as the ratio of the post-collisional to pre-collisional normal component of the relative velocity) for the materials involved:

$$C_n = 2\gamma\sqrt{m_{ij}k_n} \quad (4.4)$$

$$\text{where } \gamma = -\frac{\ln(\varepsilon)}{\sqrt{\pi^2 + \ln^2(\varepsilon)}}, \quad \text{and} \quad m_{ij} = \frac{m_i m_j}{m_i + m_j} \quad (4.5)$$

Discrete Element Method simulations were carried out with columns having different initial aspect ratio ' a ', varying from 0.2 to 10. In order to study the effect of crystallisation on the run-out distance, 10 more MD simulations were carried out on granular columns composed of grains arranged on a hexagonal lattice. In order to maintain a threshold amount of grains, in all the cases the columns contain at least 1000 grains, which is the safe lower limit for DEM as suggested by [Oda and Iwashita \(1999\)](#). The micro-mechanical parameters used in this study are presented in Table 4.2. Due to the unsteady nature of the flow, the grains get dispersed on

Table 4.2 Micromechanical parameters used in Discrete Element Method simulations

Parameter	Value
Young's modulus of glass bead	$70 \times 10^9 \text{ N m}^{-2}$
Poisson's ratio	0.22 - 0.24
Diameter of glass beads	0.92 to 1.38 mm
Normal and shear stiffness of grains	$1.6 \times 10^8 \text{ N m}^{-1}$
Normal and shear stiffness of wall	$4 \times 10^8 \text{ N m}^{-1}$
Inter-particle friction coefficient, μ	0.53
Wall friction coefficient	0.466
Coefficient of restitution, Γ	0.6

Table 4.3 Parameters used in continuum simulations

Parameter	Value
Number of material points representing an actual particle	4
Material point spacing	0.575 mm
Number of material points per mesh	16
Young's Modulus, E	$1.98 \times 10^6 \text{ Pa}$
Poisson's ratio, ν	0.22 to 0.24
Friction angle, ϕ	23.0°
Dilatancy angle, Φ	0°
Density, ρ	1800 kg m^{-3}
Wall friction	0.466
Time step increment	$1.0 \times 10^{-6} \text{ s}$

¹ the horizontal plane as discrete bodies start to separate from the main mass, hence the run-out
² distance is calculated as the position of the farthest grain which has at least one contact with the
³ main mass. A plane strain collapse of granular column is simulated as a continuum using MPM.
⁴ The effect of number of material points on the accuracy of the simulation was discussed in
⁵ Chapter 4. [Guilkey et al. \(2003\)](#) suggests at least four particles per cell for problems involving
⁶ large deformations. 10 MPM simulations of the granular column collapse were performed using
⁷ Mohr-Coulomb constitutive law by varying the initial aspect ratio, to understand the difference
⁸ between the particle and continuum scale description of granular flows. The parameters used
⁹ for the continuum analyses are presented in Table. 4.3. The Young's modulus of the granular
¹⁰ assembly is determined by performing a uni-axial compression of the granular column in
¹¹ Discrete Element Method.

4.2.1 Deposit morphology

The variation of the normalized final run-out distance, $\Delta L = (L_f - L_i)/L_i$, with the initial aspect ratio ‘a’ of the column is presented in Figure 4.4. Similar to the experimental results, a power law relationship is observed between the normalized run-out distance and the initial aspect ratio of the column. However, the molecular dynamics simulations with random packing of grains overestimate the run-out distance by a factor of 1.2. In the present study, the following scaling law for the run-out is observed.

$$\frac{L_f - L_i}{L_i} \approx \begin{cases} 1.67a, & a \lesssim 2.3 \\ 2.5a^{2/3}, & a \gtrsim 2.3 \end{cases} \quad (4.6)$$

The run-out distance observed in the case of hexagonal packing of grains matches the experimental run-out distance observed by [Lajeunesse et al. \(2004\)](#). However, the Discrete Element Method simulations performed with random packing predict longer run-out distances in comparison with the experimental data. The difference in the run-out distance can be attributed to the variation in the packing of grains in the granular column. Although, experimental data corresponds to granular column collapse in a rectangular channel, the collapse is not a pure two-dimensional collapse as in the case of numerical simulations. This can cause some variation in the run-out distance. [Balmforth and Kerswell \(2005\)](#) observed that the material property affects the final run-out distance and included a pre-factor ‘ λ ’ in the scaling law, which is in contrast to the observation made by [Lube et al. \(2005\)](#). The scaling law observed in the present study for the random packing is identical to the scaling law observed by [Lajeunesse et al. \(2004\)](#), except for the pre-factor in the scaling law, indicating a strong correlation between the run-out distance and the material property. [Daerr and Douady \(1999\)](#) also observed the effect of initial packing density and the internal structure on the behaviour of granular flows. The continuum description of the granular column collapse using Material Point Method shows good agreement with the experimental results for columns with lower aspect ratio (‘ a ’ $\lesssim 2.3$), however it exhibits a significant increase in the run-out distance beyond the aspect ratio of 2.3. [Bandara \(2013\)](#) also observed a jump in the run-out distance at the initial aspect ratio of 2.

In order to understand the mechanism of the run-out in a granular column collapse, it is essential to study the relation between the final collapsed height of the granular column and its initial aspect ratio. Figure 4.5 shows the variation of the normalized final height with the initial aspect ratio of the column. The final height predicted by the Discrete Element Method and the MPM simulations matches the experimental data for granular columns with aspect ratio below 0.7, which indicates that the initial density of the column has negligible effect on the final collapse height. The scaling of final height of the column with the initial aspect ratio of

1 the column can be written as:

$$2 \quad \frac{H_f}{L_i} \propto \begin{cases} a, & a \lesssim 0.7 \\ 3 \quad a^{2/3}, & a \gtrsim 0.7 \end{cases} \quad (4.7)$$

4 The Material Point Method predicts a higher final height of the column in comparison with
5 the particular simulations that should result in shorter run-outs, however it is inconsistent with
6 the observations. In case of granular columns with smaller aspect ratios, only a tiny portion of
7 the total mass is mobilized and the rest remains static, thus predicting the final collapse height
8 accurately. The final height of a column is controlled by the amount of static region in the
9 granular column collapse, while the run-out distance is essentially a function of the flowing
10 mass. Hence, it is essential to compare the evolution of flow and the internal flow structure
11 in the Discrete Element Method and Material Point Method simulations to understand the
12 limitations of both the continuum and discrete element approaches.

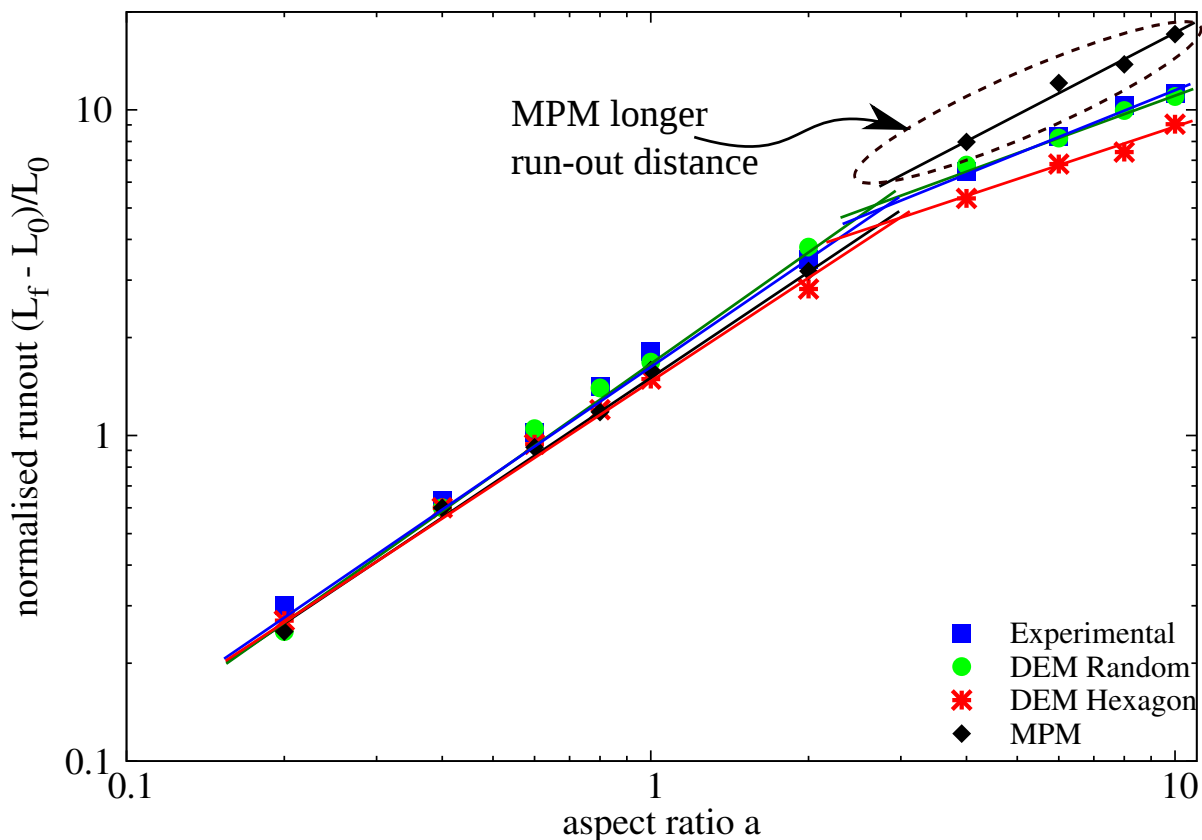


Figure 4.4 Normalised final run-out distance for columns with different initial aspect ratio

4.2 Granular column collapse

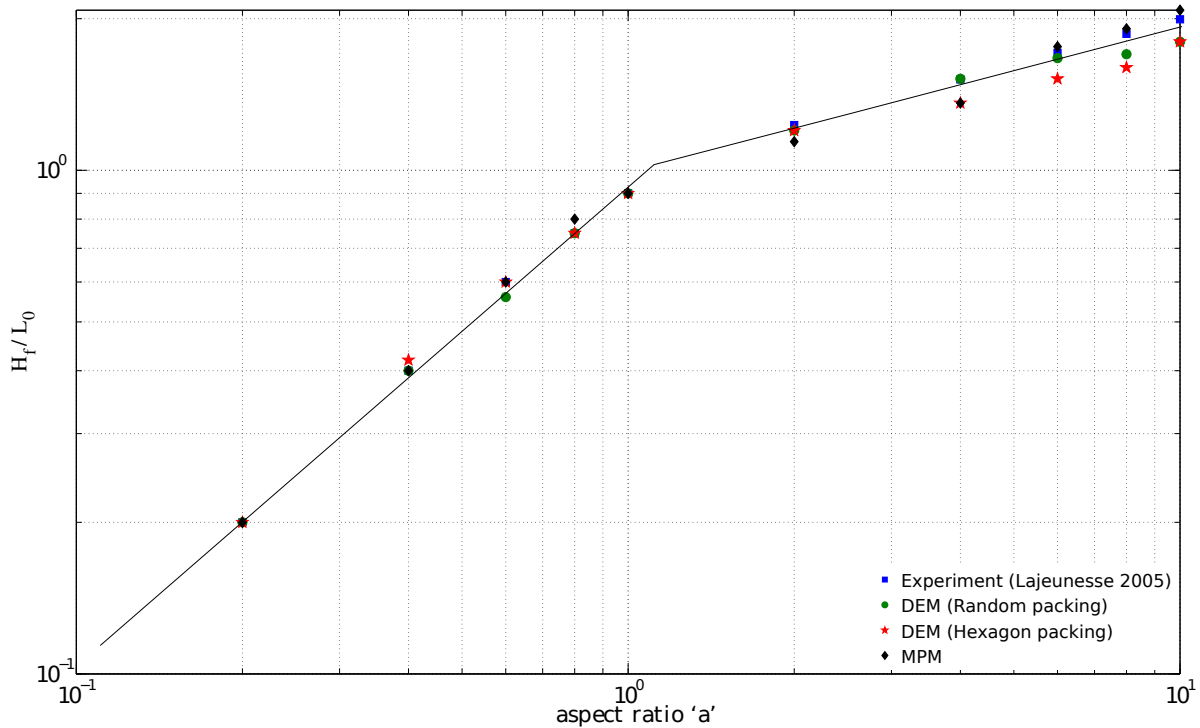


Figure 4.5 Normalised final collapse height for columns with different initial aspect ratio

4.2.2 Flow evolution and internal flow structure

For a fixed granular material and substrate properties, the flow dynamics and the final deposit morphology do not depend on the volume of granular material released, but depend only on the aspect ratio ‘ a ’ of the column. A power law relationship is observed between the run-out distance and the initial aspect ratio of the column. A transition in the run-out behaviour at an aspect ratio of 2.3 indicates a change in the flow dynamics. For smaller aspect ratios, the granular mass fails through avalanching of flanks producing a truncated cone-like deposit ($‘a’ < 0.7$) or conical deposit ($‘a’ > 0.7$). At smaller values of aspect ratios, the flow is initiated by failure at the edge of the pile along a well-defined fracture surface. The grains located above the failure surface move “*en masse*” leaving a static region underneath the failure surface. After a transient time of order τ_c , defined as $\sqrt{H_i/g}$, the flow is fully developed. The velocity profile along the granular column at critical time τ_c is presented in Figure 4.6. At critical time, the velocity field depends only on the position of the grain along the sliding mass. The maximum velocity is observed at the front of the flowing mass corresponding to that of a plug flow in horizontal direction. Particulate and continuum simulations yield similar run-out distance at critical time. Unlike particulate simulations, the Material point method predicts that the maximum horizontal velocity occurs at the top of the sliding mass. Behind the fast flowing

1 front, the flow is localized in the mass above the failure surface and the velocity profiles are
2 locally parallel to the failure plane. The flow is composed of upper linear part and a lower
3 exponential tail in the static granular bed. The velocity profile is similar to steady granular
4 surface flow as observed by [Lajeunesse et al. \(2004\)](#).

5 For columns with lower initial aspect ratios, the run-out distance is proportional to the
6 mass flowing above the failure surface. To understand the amount of mass mobilized during a
7 collapse, the angle of the failure surface has to be studied. Figure 4.6 shows a distinct failure
8 surface when the flow is fully developed at critical time τ_c . The angle of the failure surface is
9 found to be about 55° . The failure surface begins from the toe of the column and protrudes
10 inwards at an angle of 50 to 55° . For columns with lower aspect ratios, the formation of
11 the “truncated conical deposit” or “conical deposit” depends only on the initial length of the
12 column, as the angle of the failure surface is found to be independent of the aspect ratio. The
13 failure angle is consistent with the interpretation in terms of *active Coulomb failure* ([Lajeunesse et al., 2004](#)), which leads to a predicted failure angle $\theta_y = 45^\circ + \delta/2$, where δ is the internal
14 friction angle of the granular material. In the present study, the friction angle of the glass
15 beads is 22° , which leads to $\theta_y = 45^\circ + 22^\circ/2 = 56^\circ$, which is in good agreement with the
16 numerical simulations and experimental observations by [Lajeunesse et al. \(2004\)](#). Contrary to
17 the suggestion of [Lajeunesse et al. \(2004\)](#), the fracture angle is found to have no direct effect
18 on the transition between the truncated cone and the conical deposit occurring at an aspect ratio
19 of 0.7 . [Schaefer \(1990\)](#) observed the onset of instabilities in a narrow wedges of 56 to 65° for
20 Cambridge type constitutive models that describes granular flows. This observation matches
21 well with the failure angle observed in the present study. The final profile of the collapsed
22 granular column with an initial aspect ratio of 0.4 is shown in Figure 4.7. The failure surface is
23 distinct and the hexagonal dense packing of grains has a steeper failure surface in comparison
24 with the random packing. The variation observed in the angle of the failure surface causes a
25 difference in the amount of mobilized mass above the failure surface, and in turn in the run-out
26 distance. The lower value of run-out distance observed in the case of hexagonal packing of
27 grains can be attributed to the crystallisation effects. crystallisation is the formation of large-
28 scale lattice structures during the flow, resulting in non-generic flow patterns. crystallisation is
29 found to have a significant effect on the final state of the granular column. [Lacaze and Kerswell \(2009\)](#)
30 observed that poly-disperse grains have lesser tendency to crystallize especially in the
31 case of columns with larger aspect ratio.

33 For larger aspect ratios, the flow is still initiated by a well defined failure surface as can be
34 seen in Figure 4.8. However, in this case the initial granular column is much higher than the
35 top of the failure surface. Due to gravity most of the grains in the column fall in the vertical
36 direction consuming the column along their way. When they reach the vicinity of the failure

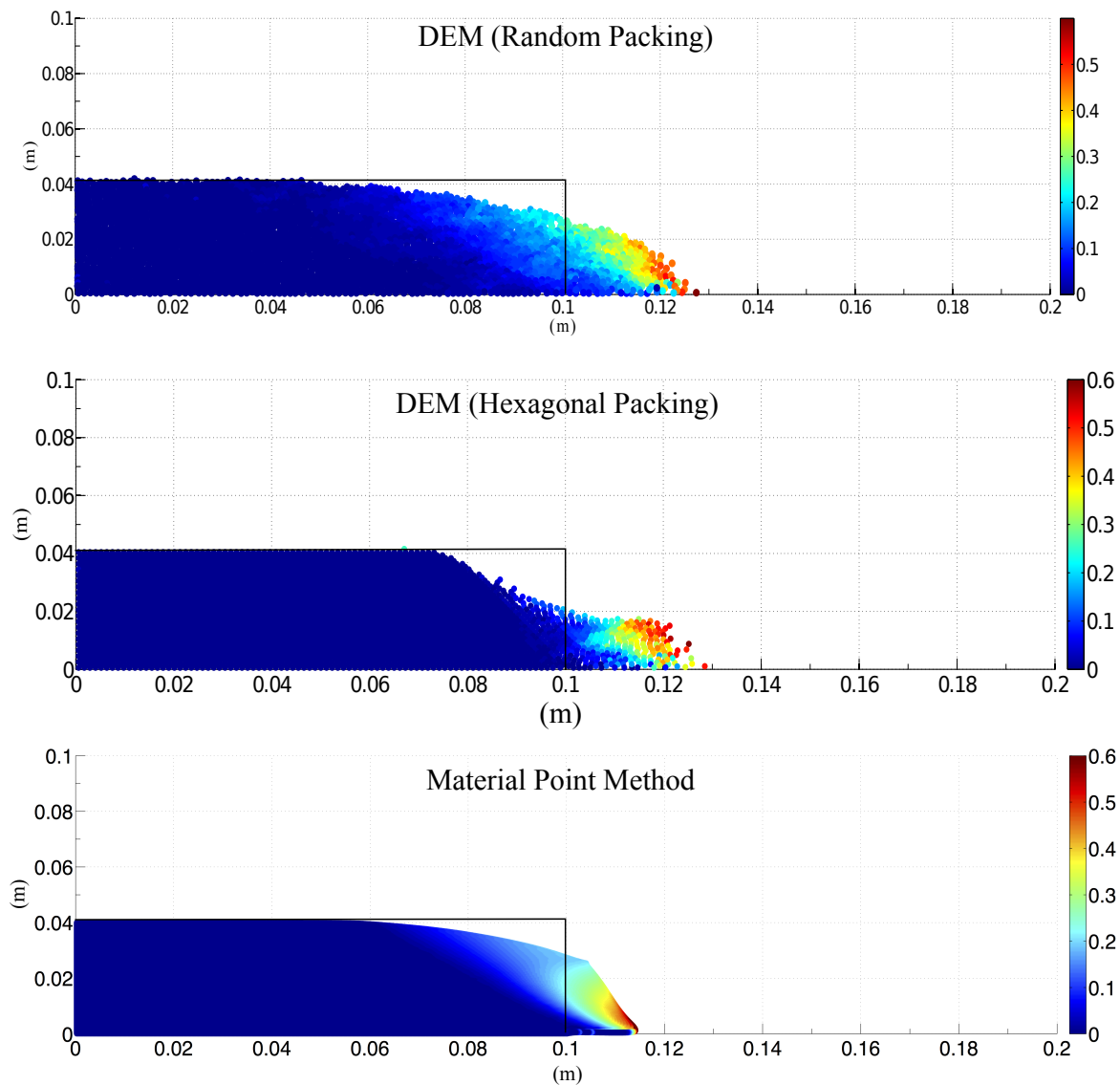


Figure 4.6 Velocity profile of a granular column collapse ($a' = 0.4 \& t = \tau_c$)

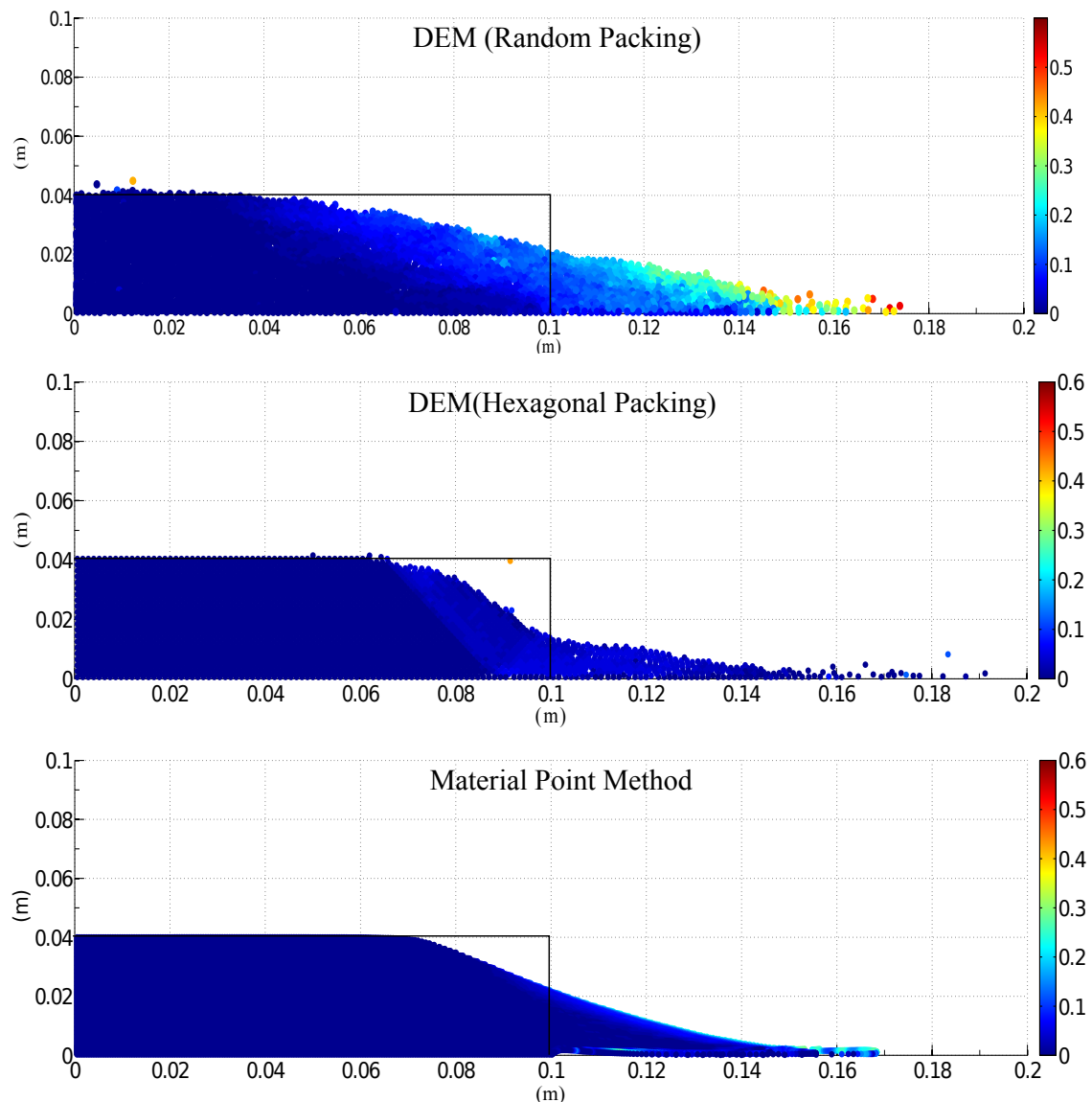


Figure 4.7 Velocity profile of a granular column collapse ($a' = 0.4 \& t = 3 \times \tau_c$)

surface, the flow gets deviated along the horizontal direction releasing a huge amount of kinetic energy gained during the free fall. For larger aspect ratio ($a > 0.7$), the resulting static region is a cone, the final height of the cone, i.e., H_f lies above the summit of the failure surface. Hence, a different evolution is observed from that of the axis-symmetric geometry (Lube et al., 2005), where the final height coincides with the summit of the failure surface forming a truncated conical deposit. Lajeunesse et al. (2004) articulated the variation in the deposit morphology between the axis-symmetric case and the rectangular collapse to be a geometrical effect rather than as an experimental artefact. The final profile of the collapsed granular column with an initial aspect ratio of 6 is presented in Figure 4.9. An initial failure surface starting from the toe end of the column at an angle of about 55° can be observed at critical time τ_c . As the collapse of the granular collapse progresses, successive failure planes parallel to the initial failure surface are formed and shear failure occurs along these planes. The presence of several shear bands in the final profile of the collapsed granular column confirms the hypothesis. Crystallisation in hexagonal packing causes a significant effect on the run-out distance by forming series of parallel shear bands. However, the Material Point Method fails to capture the formation of shear bands during the collapse. This observation throws light on the mechanics of propagation of shear bands in massive landslides such as the Storegga submarine landslide. The flow behaviour becomes similar to that of columns with lower aspect ratio as the flow starts descending along the failure plane. Regardless of the experimental configuration and the initial aspect ratio of the columns, the flow is initiated by a well-defined rupture surface, above which the material slides down leaving a static region underneath the failure plane. Depending on the aspect ratio of the column, two asymptotic behaviours are observed. For smaller aspect ratios, the flow is dominated by friction and by the pressure gradient for larger aspect ratio.

To study the flow dynamics of granular columns with different aspect ratios, the flow front $L(t)$ and the maximum height of column $H(t)$ are tracked. The evolution of scaled height (H_f/L_i) and the run-out distance $(L_f - L_i)/L_i$ with time for granular columns with an initial aspect ratio of 0.4 and 6 are presented in Figures 4.10 and 4.11. Time is scaled with respect to the critical time τ_c , defined as the time at which the flow is fully mobilized. Three distinct regions can be observed in the flow evolution of granular column collapse regardless of the initial aspect ratio of the column. An initial transient acceleration phase is observed for a time $0.8\tau_c$. This phase is followed by a heap movement of granular materials at the foot with a constant spreading velocity V for about $2\tau_c$. When time ' t ' > τ_c , the velocity varies linearly with depth in the flowing layer and decreases exponentially with depth near the static layer. This velocity profile is similar to those observed in steady granular surface flows (Lajeunesse et al., 2004). Most of the run-out happens during this phase. The final phase involves deceleration of the flow front and the flow comes to rest after $0.6\tau_c$. The spreading of the granular column ceases after a time

in the order of $3\tau_c$ for all values of aspect ratios, however some motion still persists along the free surface behind the flow front for a much longer time due to internal rearrangement, the duration of which can last up to $t \approx 6\tau_c$. For smaller aspect ratios, the critical time is evaluated as the point of intersection of the scaled run-out and height. The critical time predicted for both hexagonal and random packing of grains matches the experimental observations. However, the Material Point Method overestimates the critical time by a factor of 1.25, which means that it takes longer for the flow to be fully mobilized. However, the actual run-out duration is short and the granular materials comes to rest abruptly at about $t = 3\tau_c$. For columns with larger aspect ratios, the continuum and particulate approaches simulate similar flow evolution behaviour for times up to $3\tau_c$, beyond which particulate simulations stabilise and come to rest, while the flow continues to evolve in MPM simulations resulting in larger run-outs than expected. The flow tends to come to rest at time $t = 6\tau_c$. The three phases in a granular flow can be distinctly observed in the flow evolution plot for a granular column with initial aspect ratio of 6 (see Figure figure 4.11). For larger aspect ratios, the flow evolution behaviour observed in the case of random packing matches the experimental observation by Lajeunesse et al. (2004). Hexagonal packing predicts longer time for the flow to evolve, which can be attributed to the increase in the internal resistance due to crystallisation of grains. MPM overestimates the critical time by 50%, however has the same value of run-out as the particulate simulations, at time $t = 3\tau_c$, beyond which the material continues to flow until it ceases at $6\tau_c$. In order to understand the flow dynamics in the case of Material Point Method it is important to study the effect of different parameters on the deposit morphology.

4.2.3 Energy dissipation mechanism

The time evolution of the flow exhibited three distinct stages during the collapse of a granular column. Studying the energy dissipation mechanism provides useful insight into the flow dynamics. shows the time evolution of potential energy (E_p) and kinetic energy (E_k) normalized by the initial potential energy E_o .

$$E_p = \sum_{p=1}^{N_p} m_p g h_p \quad (4.8)$$

$$E_{ki} = \frac{1}{2} \sum_{p=1}^{N_p} m_p v_p^2 \quad (4.9)$$

where N_p is the total number of particles, m_p is the mass of a particle ‘ p ’, h_p is the height and v_p is the velocity of the particle ‘ p ’. It can be observed from the figure that the initial potential energy stored in the particle is converted to kinetic energy which is dissipated as the granular

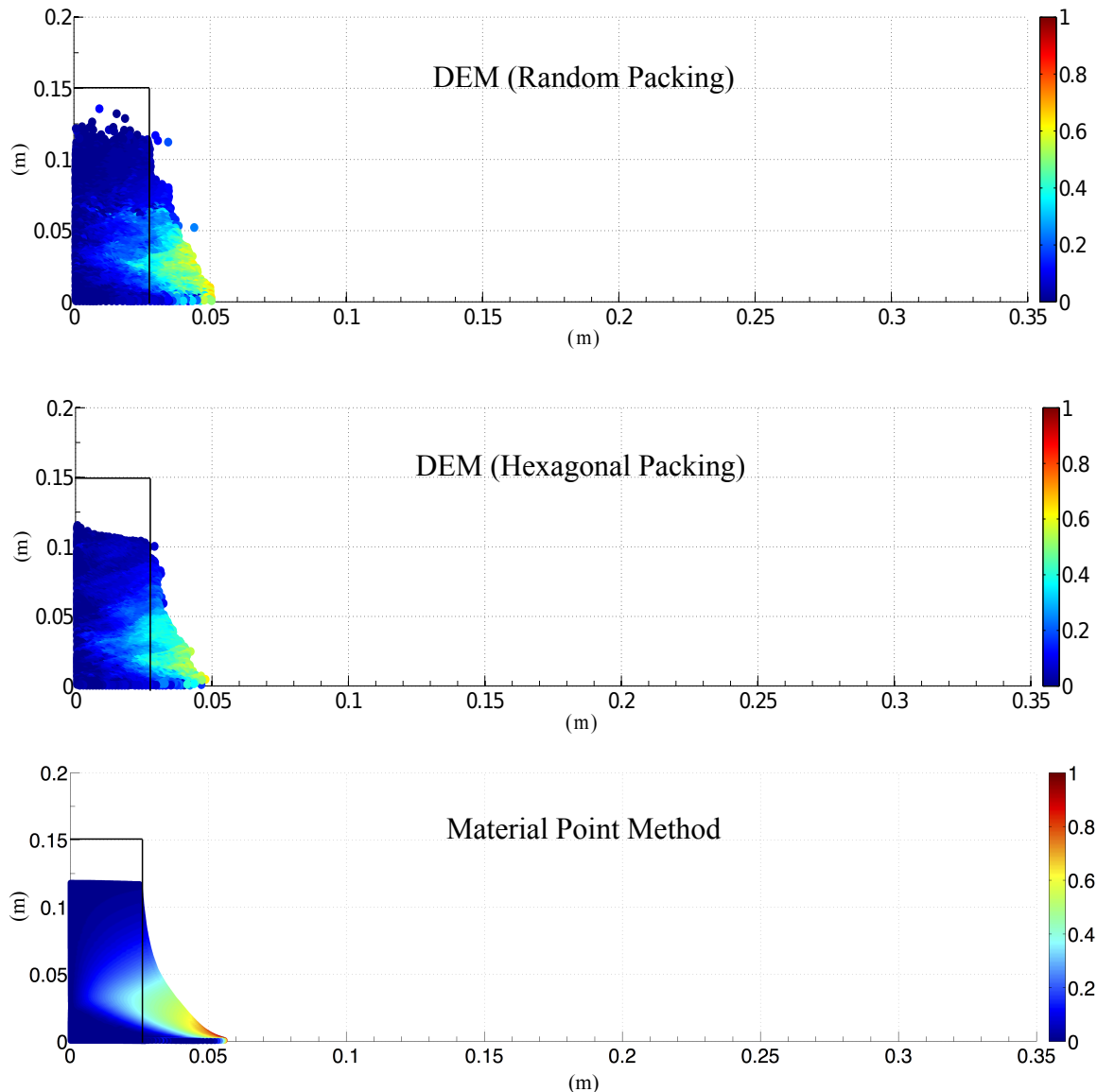


Figure 4.8 Velocity profile of a granular column collapse (' $a' = 6\& t = \tau_c')$

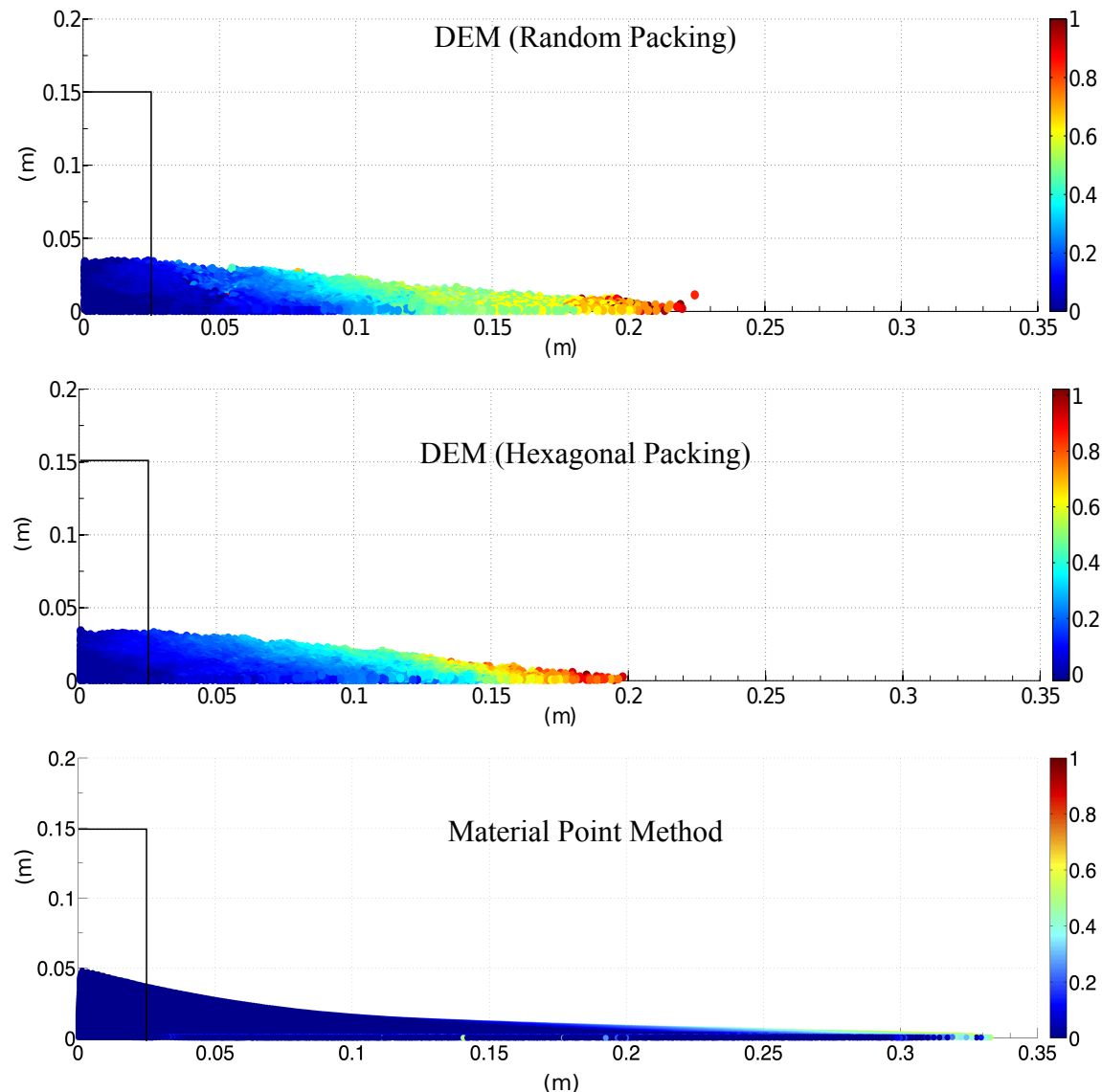
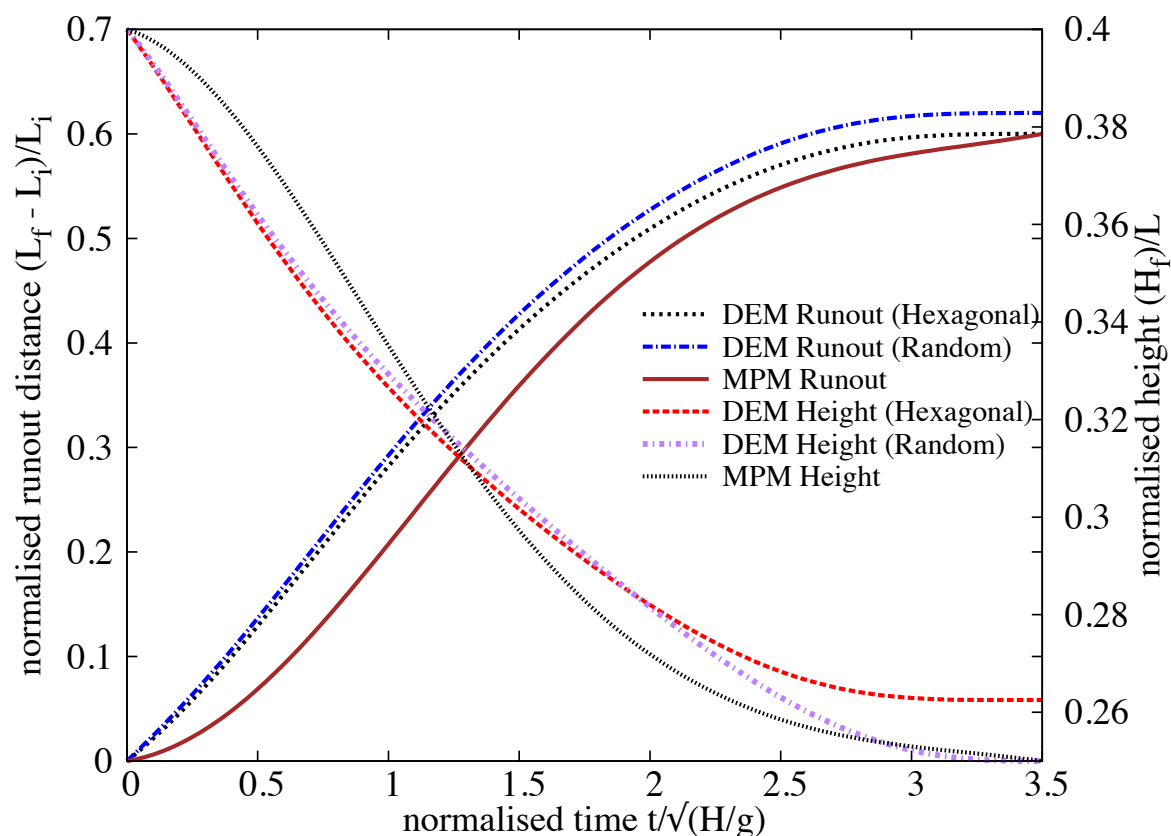
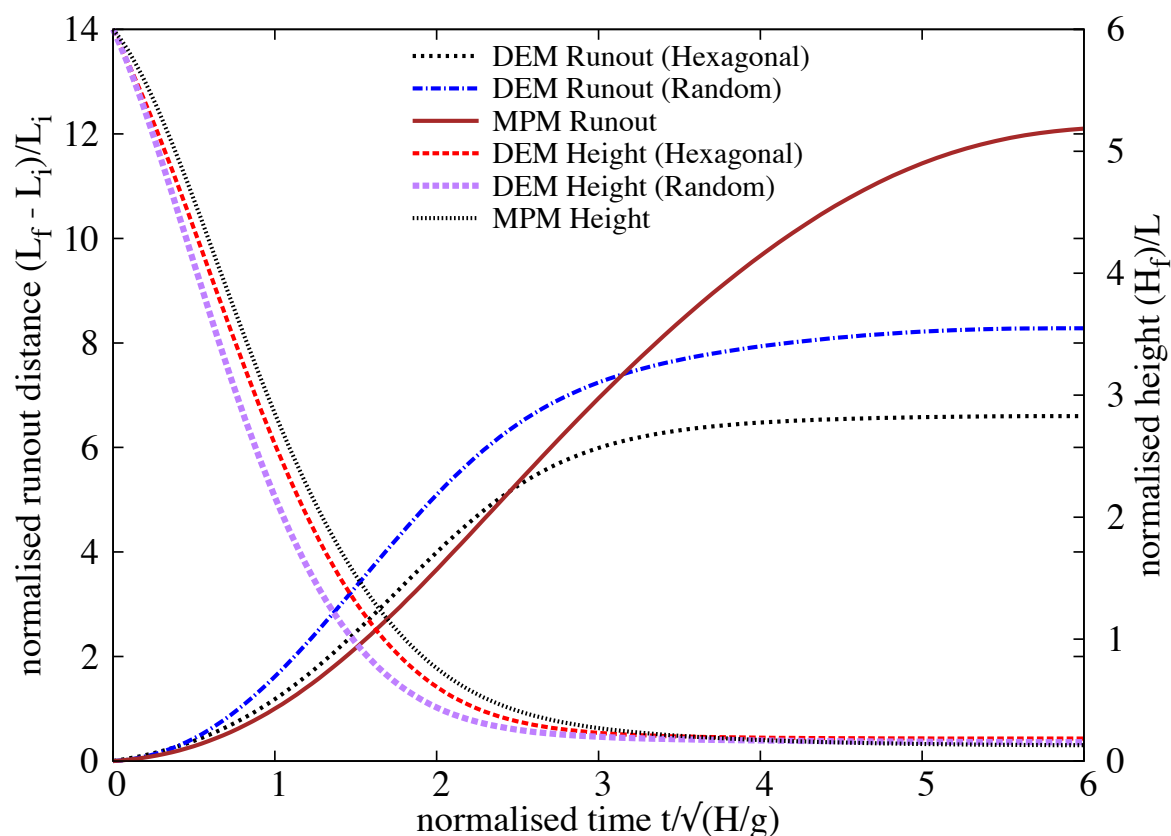


Figure 4.9 Velocity profile of a granular column collapse ($a' = 6$ & $t = 3 \times \tau_c$)

Figure 4.10 Flow evolution of a column with ' a' = 0.4

Figure 4.11 Flow evolution of a column with ' a' = 6

material flows down. Three successive stages can be identified in the granular column collapse. In the initial acceleration stage ($t < 0.8\tau_c$), the initial potential energy stored in the grains is converted into vertical motion. In the second stage, the grains undergo collisions with the bottom plane and/or with neighbouring grains, and the stored potential energy is converted into horizontal motion. In the third stage, the grains eventually leave the base area of the column and flow sideways. As the process involves collective dynamics of all the particles, it is difficult to predict the exact trajectory of a grain, however, the overall dynamics can be explained. To explain the dissipation of energy during the collapse, Staron et al. (2005) assumed that the total initial potential energy stored in the system is completely dissipated through friction over the entire run-out distance as:

$$\mu m_0 g \times (L_f - L_i) = m_0 g H_o \quad (4.10)$$

where μ is the friction coefficient. The model predicts well the flow dynamics for columns with larger aspect ratios, as most of the initial potential energy is dissipated during the collapse involving the entire column. However, for columns with smaller aspect ratios, only a portion of the mass above the failure surface is involved in the flow. Hence, the energy dissipation should involve only the grains lying above the failure surface. A mathematical model, which considers the grains lying above the failure surface, will be derived to predict the flow dynamics of the granular column collapse for different aspect ratios.

4.3 Slopes subjected to impact loading

4.3.1 Numerical procedures

The numerical samples are composed of ~ 13000 disks with a uniform distribution of diameters by volume fractions in the range $[d_{min}, d_{max}]$ with $d_{max} = 1.5d_{min}$. The mean particle diameter and mass are $d \simeq 0.0025$ m and $m \simeq 0.0123$ kg, respectively. The particles are first poured uniformly into a rectangular box of given width and then the right-hand side wall is shifted further to the right to allow the particles to spread. A half-pile is obtained when all particles come to rest; see Fig. ???. This procedure leads to a mean packing fraction $\simeq 0.83$.

The initial static pile is set into motion by applying a constant horizontal gradient $v_{0x}(y) = k(y_{max} - y)$ with $k > 0$. Such a configuration mimics the energy transfer mechanism of a horizontal quake along the bottom of the pile. We are interested in the evolution of the geometry of the pile and its total kinetic energy as a function of the initial input energy E_0 . The run-out distance R_f is the distance of the rightmost particles from the left wall when the pile comes to rest. It will be normalized by the initial extension R_0 of the pile, as in the experiments

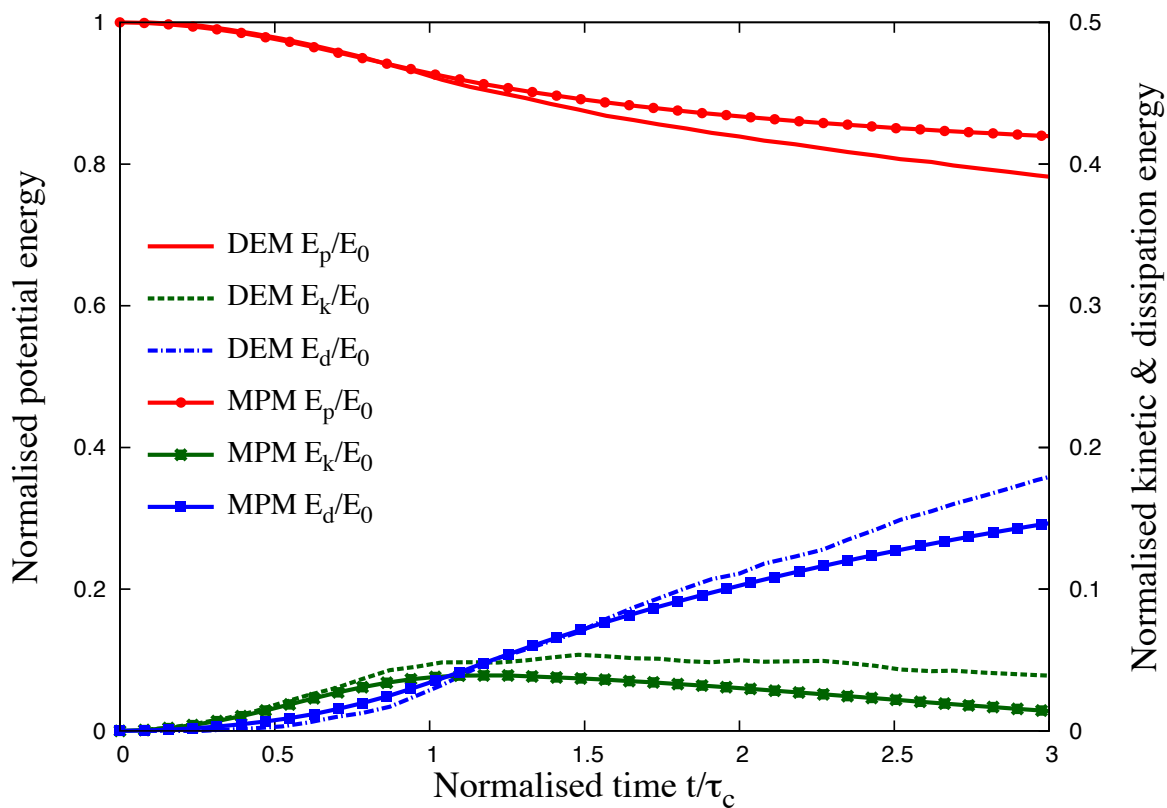
Figure 4.12 Energy evolution of a column with ' a' = 0.4

Figure 4.13 Energy evolution of a column with ' a' = 6

1 of collapsing columns. The total run-out duration t_f is the time that the pile takes to reach its
 2 final run-out distance R_f .

3 The initial static pile is set into motion by applying a horizontal velocity $v_{0x}(y)$ to all
 4 particles during a short interval of time. Different velocity fields were tested: 1) The same
 5 velocity $v_{0x}(y) = v_0$ applied to all particles, 2) The same velocity $v_{0x}(y) = v_0$ applied to a
 6 column of particles next to the left wall, 3) a constant velocity gradient $v_{0x}(y) = k(y_{max} - y)$
 7 with $k > 0$. The first two pushing modes mimic the case of a pile impacted from the left
 8 by a moving mass (tsunami, debris...) whereas the last mode represents energy transfer by
 9 horizontal quake of the bottom line. We will compare briefly below the effect of different
 10 pushing modes, but later we will mainly explore the third mode. We are interested in the
 11 evolution of the geometry of the pile and its total kinetic energy as a function of the initial
 12 energy input E_0 . The run-out distance R_f is the distance of the rightmost particles from the left
 13 wall when the pile comes to rest. It will be normalized by the initial extension R_0 of the pile, as
 14 in the experiments of collapsing columns. The total run-out duration t_f is the time that the pile
 15 takes to reach its final run-out distance R_f .

16 For grain scale simulations, classical Discrete Element Method and Contact Dynamics
 17 approach is used. A detailed description of the Contact Dynamics method can be found in [Jean](#)
 18 ([1999](#)); [Moreau](#) ([1993](#)); [Radjai and Dubois](#) ([2011](#)); [Radjai and Richefeu](#) ([2009](#)). This method
 19 is based on implicit time integration of the equations of motion and a nonsmooth formulation
 20 of mutual exclusion and dry friction between particles. The CD method requires no elastic
 21 repulsive potential and no smoothing of the Coulomb friction law for the determination of
 22 forces. For this reason, the simulations can be performed with large time steps compared to
 23 molecular dynamics simulations. The unknown variables are particle velocities and contact
 24 forces, which are calculated at each time step by taking into account the conservation of
 25 momenta and the constraints due to mutual exclusion between particles and the Coulomb
 26 friction. We use an iterative research algorithm based on a nonlinear Gauss-Seidel scheme.
 27 The only contact parameters within the CD method are the friction coefficient μ_s , the normal
 28 restitution coefficient e_n and the tangential restitution coefficient e_t between particles. We will
 29 investigate the effect of these parameters on the evolution of kinetic energy and the profile of
 30 the pile.

31 The natural units of our system are the mean particle diameter d , mean particle mass m
 32 and gravity g . For this reason, in the following we normalize the lengths by d , the times by
 33 $(d/g)^{1/2}$, the velocities by $(gd)^{1/2}$ and the energies by mgd . Video samples of the simulations
 34 analyzed in this paper can be found by following the link <http://www.cgp-gateway.org/ref018>.

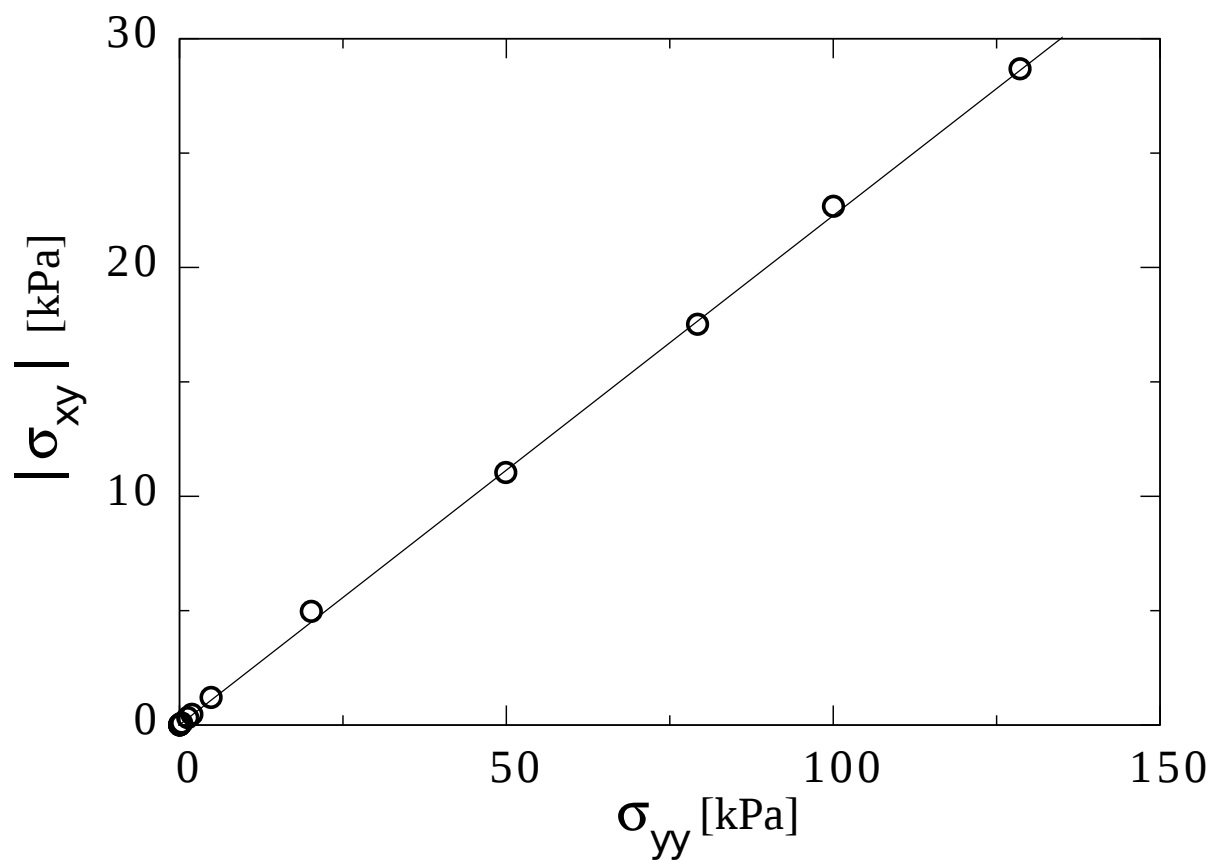


Figure 4.14 Evaluating the critical state friction angle from a periodic shear test

1 4.3.2 Evolution of pile geometry and run-out

2 In this section, we consider the spreading process following the initial energy input into the pile.
3 Fig. ?? shows several snapshots of the pile for an initial input energy $E_0 = 61$ (in dimensionless
4 units). The pile is sheared from the bottom to the top, thus leaving a cavity in the vicinity of
5 the left wall. The cavity is partially filled while the pile continues to spread to the right.

6 In this section, we consider the spreading process following the initial energy input into the
7 pile. Fig. ?? shows several snapshots of the pile for each pushing mode and for the same initial
8 energy $E_0 = 61$ (in dimensionless units). In mode 1, where the same velocity is imparted to all
9 particles, the whole pile moves away from the left wall over a short distance and then it spreads
10 out and declines in slope. The spreading continues farther until the slope nearly declines to
11 zero. In mode 2, where the velocity is applied to a column of particles next to the left wall, the
12 particles belonging to the column are literally expelled from the pile. They fall back farther
13 way on the pile after a ballistic travel above the pile. At the same time, the right side of the pile
14 slightly spreads away while the left side is filled by the particles rolling down into the gap left
15 by the column. In mode 3, the pile is sheared from the bottom to the top, leaving thus a cavity
16 in the vicinity of the left wall. The cavity is partially filled while the pile continues to spread.

17 All pushing modes involve a transient with a sharp change of the geometry of the pile
18 followed by continuous spreading to the right. In mode 2, most of the energy is carried away by
19 the ejected particles. In mode 1, the pile has a rigid-body velocity component and moves away
20 from the left wall, but shows an efficient energy transfer leading to a long run-out distance. The
21 transient is more energy consuming in mode 3 compared to mode 1. For this reason, the run-out
22 distance in mode 3 is long but shorter than in mode 1. In the following, we analyze in more
23 detail the evolution of the pile in mode 3, which mimics a horizontal quake from the bottom
24 and, despite the creation of a cavity, remains always in contact with the left wall irrespective of
25 the input energy.

26 Figure 4.4 shows the normalized run-out distance $(R_f - R_0)/R_0$ and total run-out time t_f as
27 a function of the input energy E_0 . We observe two regimes both characterized by a power-law
28 run-out distance and time as a function of E_0 . In the first regime, corresponding to the range of
29 low input energies $E_0 < 40 \text{ mgd}$, the run-out distance varies as $R_f \propto (E_0)^\alpha$ with $\alpha \simeq 0.61 \pm 0.04$
30 over nearly one decade while the duration keeps a constant value $t_f \simeq 60 (d/g)^{0.5}$ irrespective
31 of the value of E_0 ! The error on the value of the exponent represents the confidence interval
32 of linear fits on the logarithmic scale. An average run-out speed can be defined from the ratio
33 $v_s = (R_f - R_0)/t_f$. According to the data, we have $v_s \propto (E_0)^{0.61 \pm 0.04}$. Since the initial average
34 velocity varies as $v_0 \propto (E_0)^{0.5}$, this difference between the values of the exponents suggests
35 that the mobilized mass during run-out declines when the input energy is increased. As we

shall see below, the constant run-out time reflects also the collapse of the particles into the cavity left behind the pile.

In the second regime, corresponding to the range of high input energies $E_0 > 40 \text{ mgd}$, the run-out distance varies as $R_f \propto (E_0)^{\alpha'}$ over one decade with $\alpha' \simeq 0.77 \pm 0.03$ while the duration increases as $t_f \propto (E_0)^{\beta'}$ with $\beta' \simeq 0.21 \pm 0.04$. Hence, in this regime the average run-out speed varies as $v_s \propto (E_0)^{0.56 \pm 0.07}$. This exponent is close to the value 0.5 in $v_0 \propto (E_0)^{0.5}$, and hence, within the confidence interval of the exponents, in the second regime we may assume $\beta' \simeq \alpha' - 0.5$ and $v_s \propto v_0$.

It is worth noting that a similar power-law dependence of the run-out distance and time were found in the case of collapsing columns of grains with respect to the initial aspect ratio Topin et al. (2012). In the column geometry, the particles spread away owing to the kinetic energy acquired during gravitational collapse of the column. Topin et al. found that the run-out distance varies as a power law of the available peak kinetic energy at the end of the free-fall stage with an exponent $\simeq 0.5$. This value is below those obtained here for both regimes. This is, however, physically plausible since the distribution of particle kinetic energies at the end of the collapse is more chaotic than in our simulations where the energy is supplied from the very beginning in a well-defined shear mode. As pointed out by Staron et al. (2005), the distribution of kinetic energies is an essential factor for the run-out distance.

4.3.3 Decay of kinetic energy

The non-trivial evolution of the pile geometry in two regimes suggests that the energy supplied to the pile is not simply dissipated by shear and friction with the bottom plane. We also need to split the kinetic energy into its different components (x , y and rotation) of the velocity field. The input energy is in the x component, but due to both the creation of a cavity next to the left wall and the rolling of the particles down the free surface of the pile and between particles, a fraction of the energy is first transferred to the y component of the velocity field and dissipated during the transient. In this section, we analyse these features in order to arrive in a picture consistent with the evolution of the pile shape.

The decay of the total kinetic energy E is displayed in Fig. ??(a) for values of the input energy E_0 . We observe an initial fast drop of E followed by a regular fall-off until the end of the run-out. This regular fall-off occurs clearly with two different functional forms, thus revealing two stages in the evolution of the pile. Fig. ??(b) shows the same plots normalized by E_0 . We see that all plots corresponding to the first regime (low energies) collapse nearly on to a single time evolution. This is consistent with the fact that, as previously shown, in this regime the run-out time t_f is independent of the input energy. In contrast, the plots corresponding to the second regime (high energies) collapse only at the beginning of run-out, i.e. for $t < t_1 \simeq 7.5 (d/g)^{0.5}$.

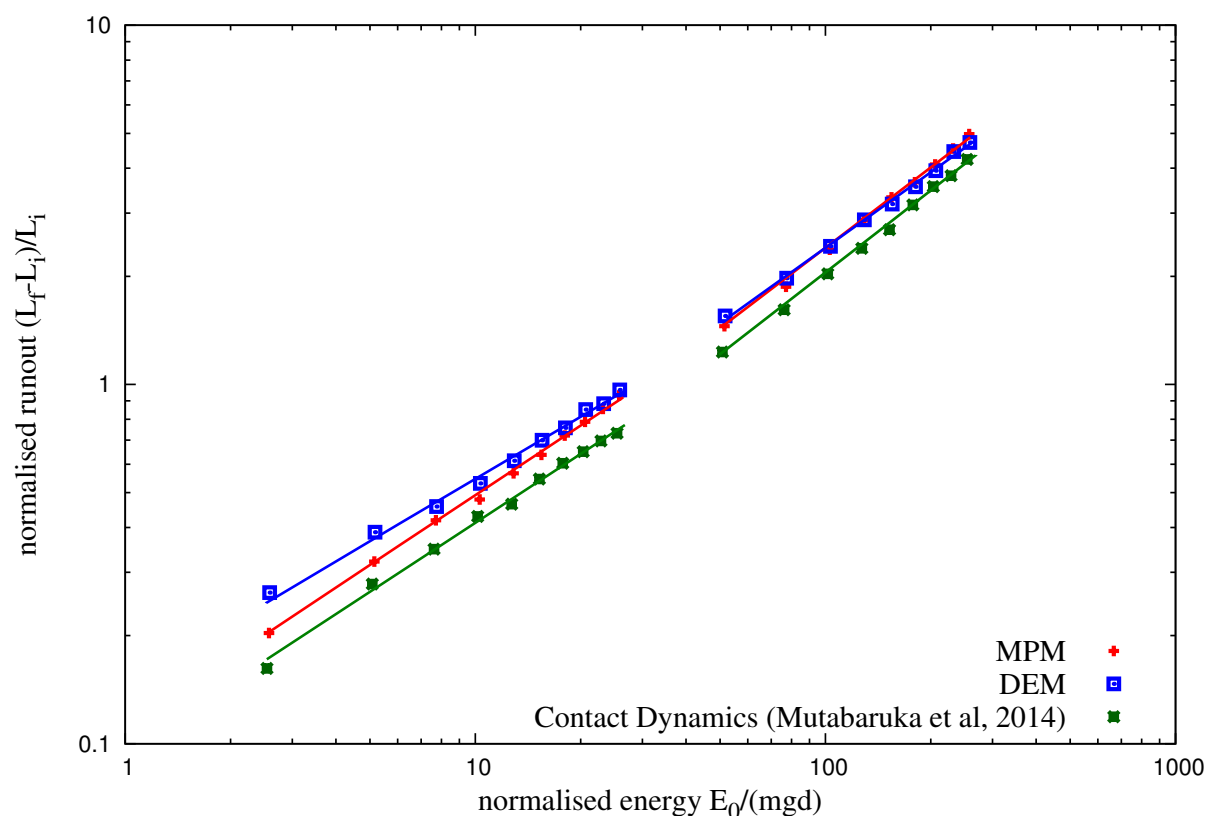


Figure 4.15 Run-out distance with normalised input kinetic energy

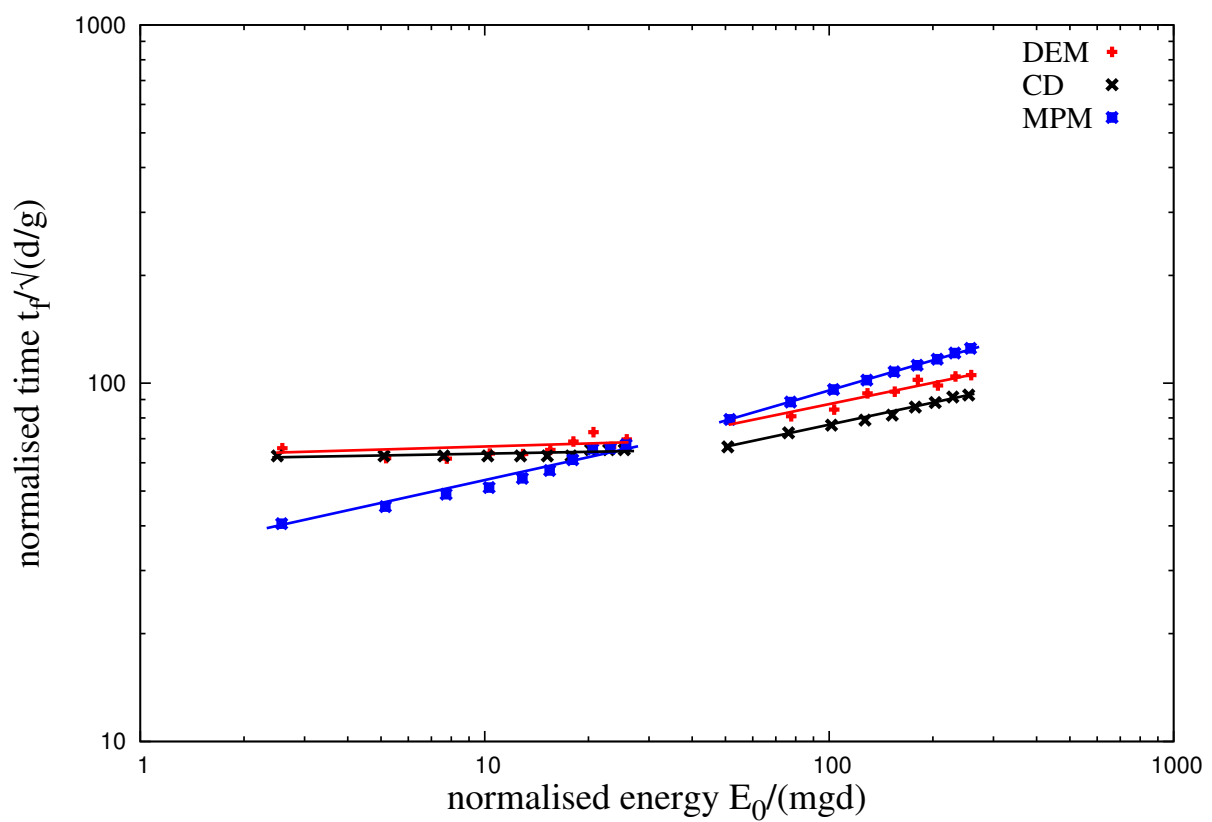


Figure 4.16 Duration of run-out with normalised input kinetic energy

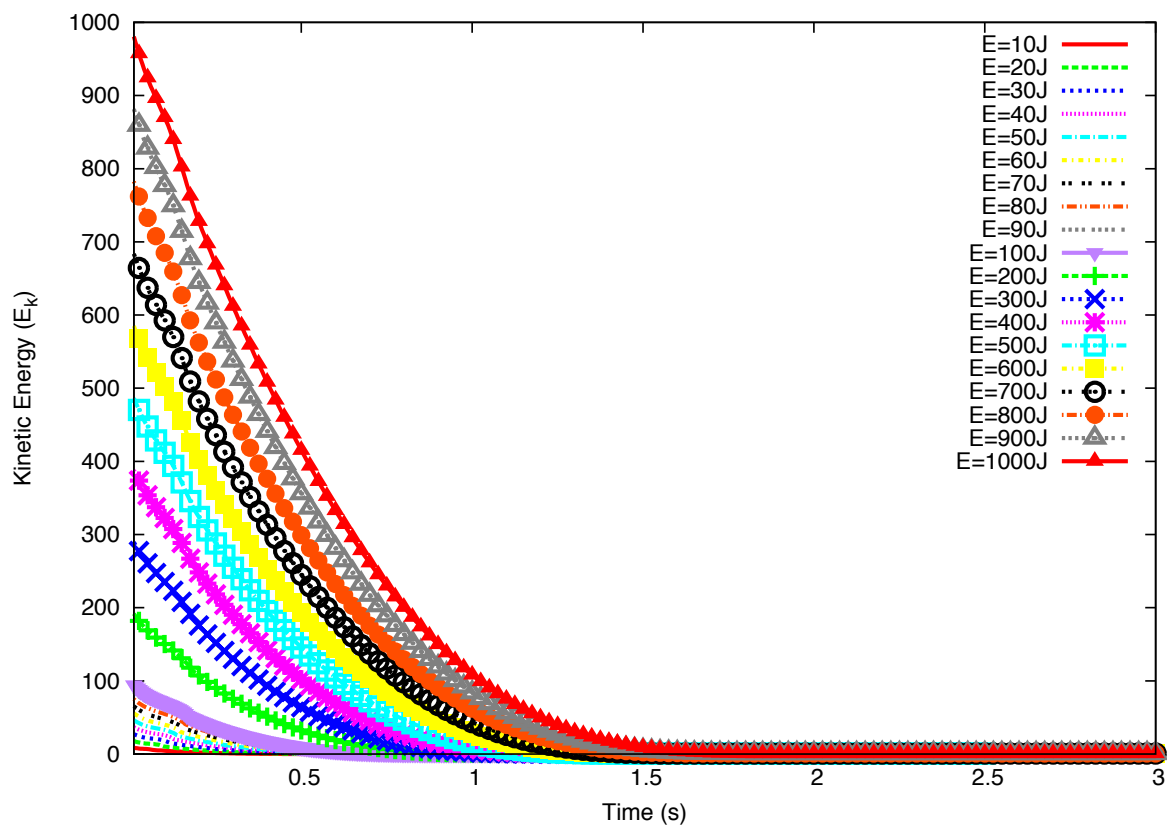


Figure 4.17 Evolution of total kinetic energy with time

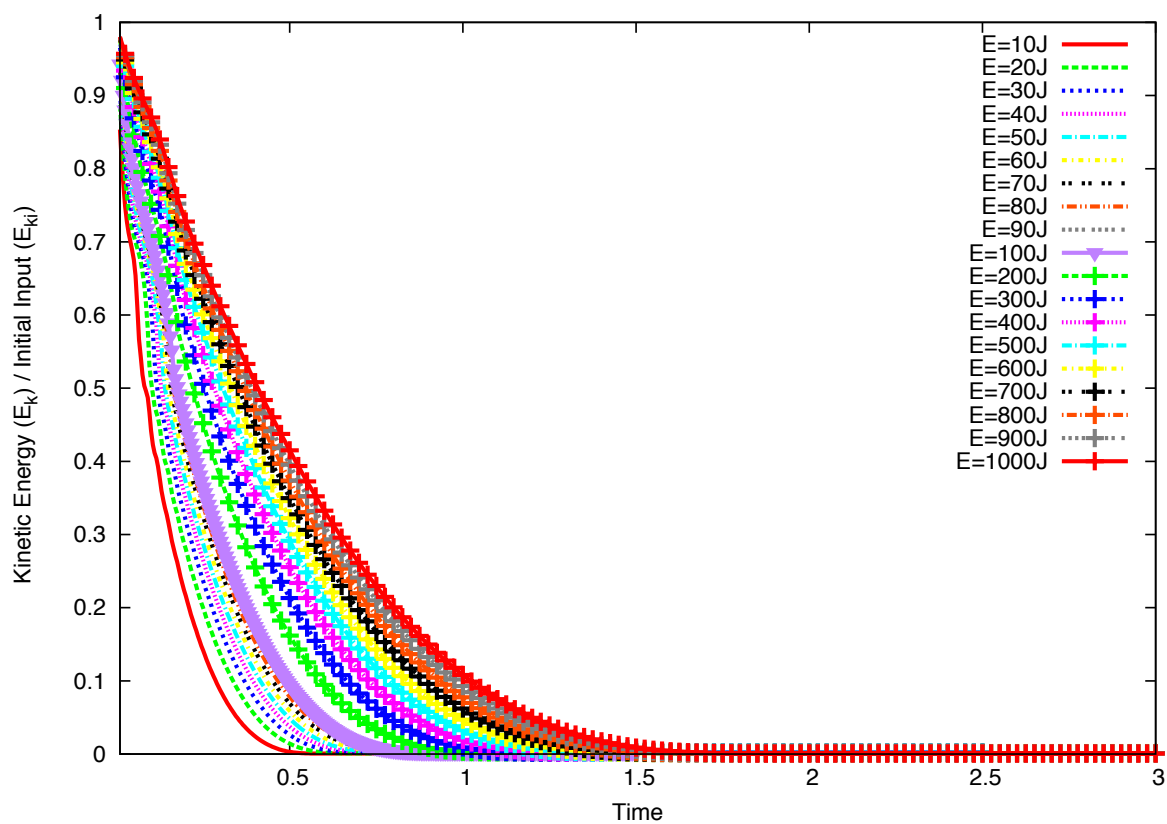


Figure 4.18 Evolution of normalised kinetic energy with time

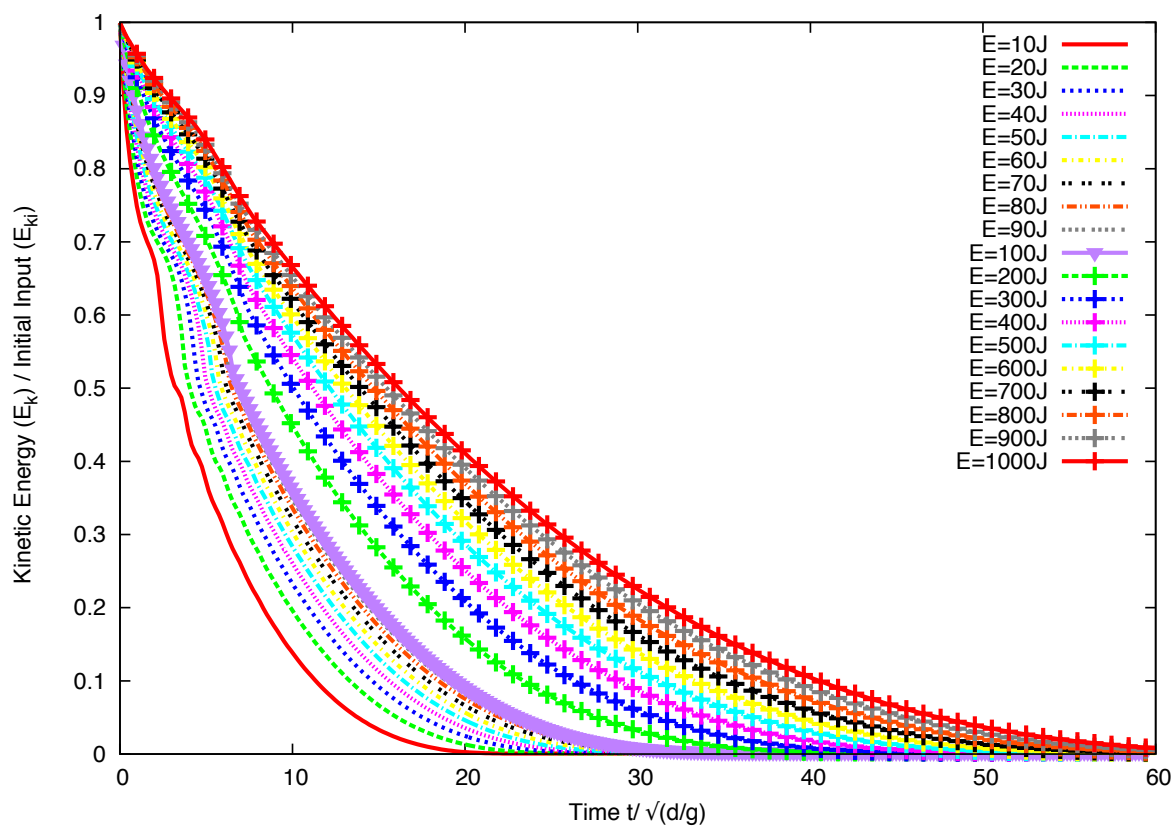


Figure 4.19 Evolution of normalised kinetic energy with normalised time

?? displays the evolution of kinetic energy in the translational (E_x and E_y) and rotational (E_θ) degrees of freedom of the particles. E_x decays as the total energy, but E_y and E_θ increase and pass through a peak before decaying rapidly to a negligibly small level. The transient is best observed for E_y , which has significant values only for $t < t_1$. This energy represents the proportion of kinetic energy transferred to the y component of the velocity field due to the destabilization of the pile and collapse of particles in the cavity behind the pile. We note that the lower E_0 , the higher the peak value of E_y/E_0 . This means that, at low values of the input energy a larger fraction of input energy E_0 is consumed in the destabilization process whereas at a high level of input energy, most of it is dissipated in the spreading phase. For this reason, the total duration t_1 of this destabilization transient is nearly the same in both regimes and its value is controlled by the gravity rather than the input energy. The height of the pile being of the order of $80 d$, the total free-fall time for a particle located at this height is $\simeq 12 (d/g)^{0.5}$, which is of the same order as t_1 . As to the rotational energy, its contribution both to the transient stage and spreading appears to be negligible.

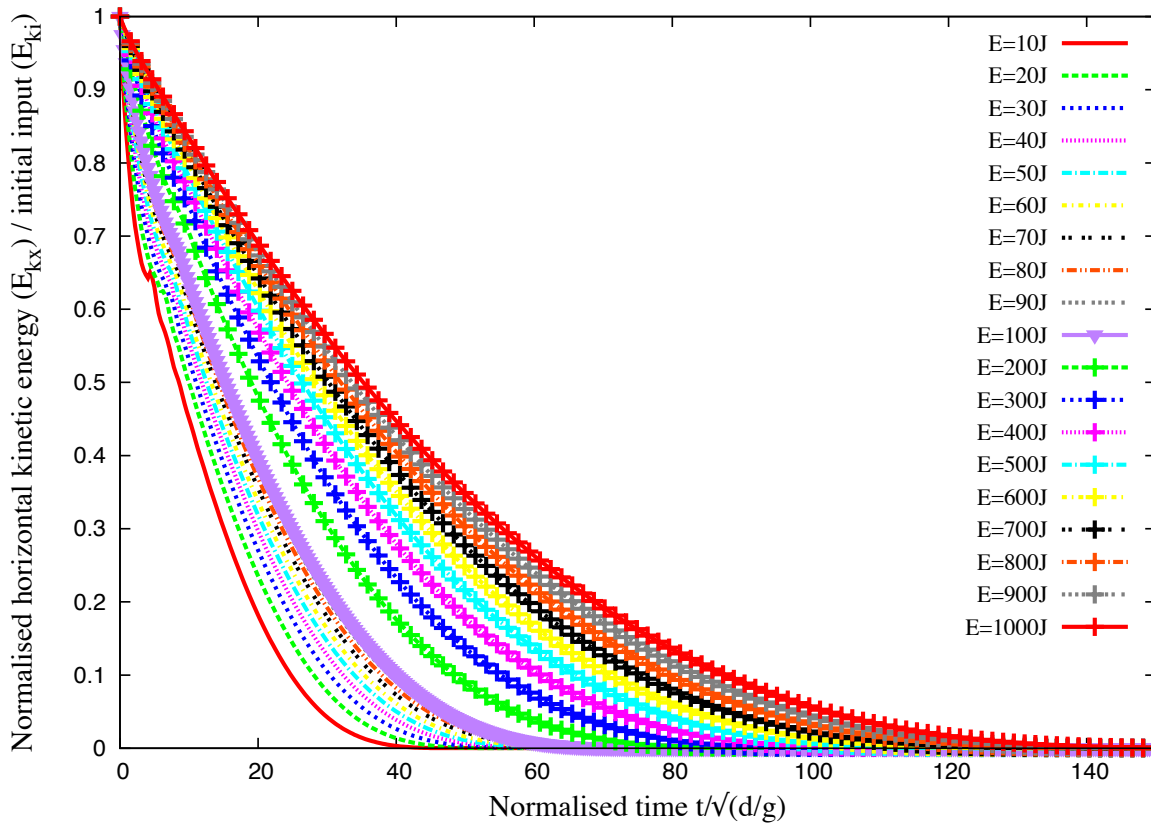


Figure 4.20 Evolution of normalised horizontal kinetic energy with time

To analyze the second phase in the second regime, we now consider only the kinetic energy E'_{x0} available at the end of the transient. This energy is responsible for most of the run-out and

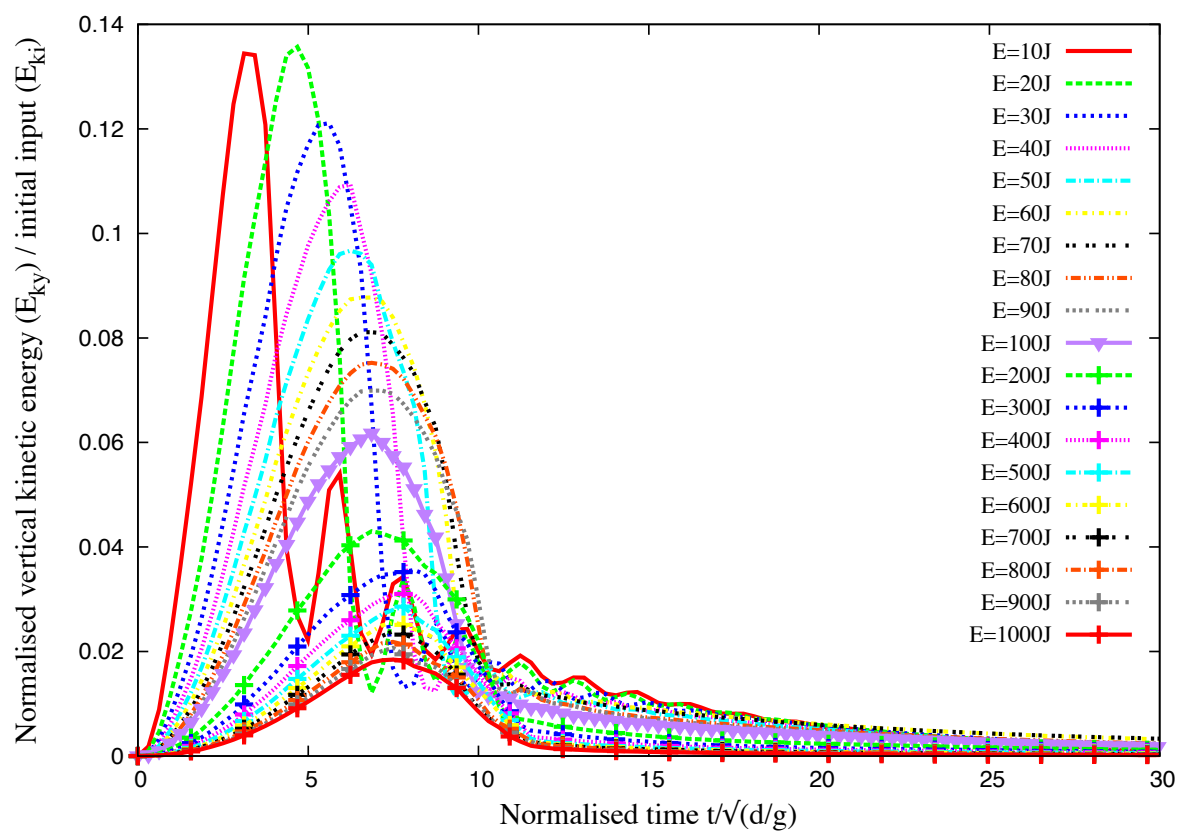


Figure 4.21 Evolution of normalised vertical kinetic energy with time

hence it is expected to control the run-out distance and time. Fig. ??(a) shows the evolution of E_x normalized by E'_{x0} as a function of time. The plots have seemingly the same aspect but they show different decay times. A decay time τ can be defined as the time required for E_x to decline by a factor 1/2. Fig. ??(b) shows the same data in which the time t' elapsed since t_1 is normalized by τ . Interestingly, now all the data nicely collapse on the same curve. We checked that this curve can not be fitted by simple functional forms such as variants of exponential decay. This means that the spreading of the pile is not a self-similar process in agreement with the fact that the energy fades away in a finite time t'_f .

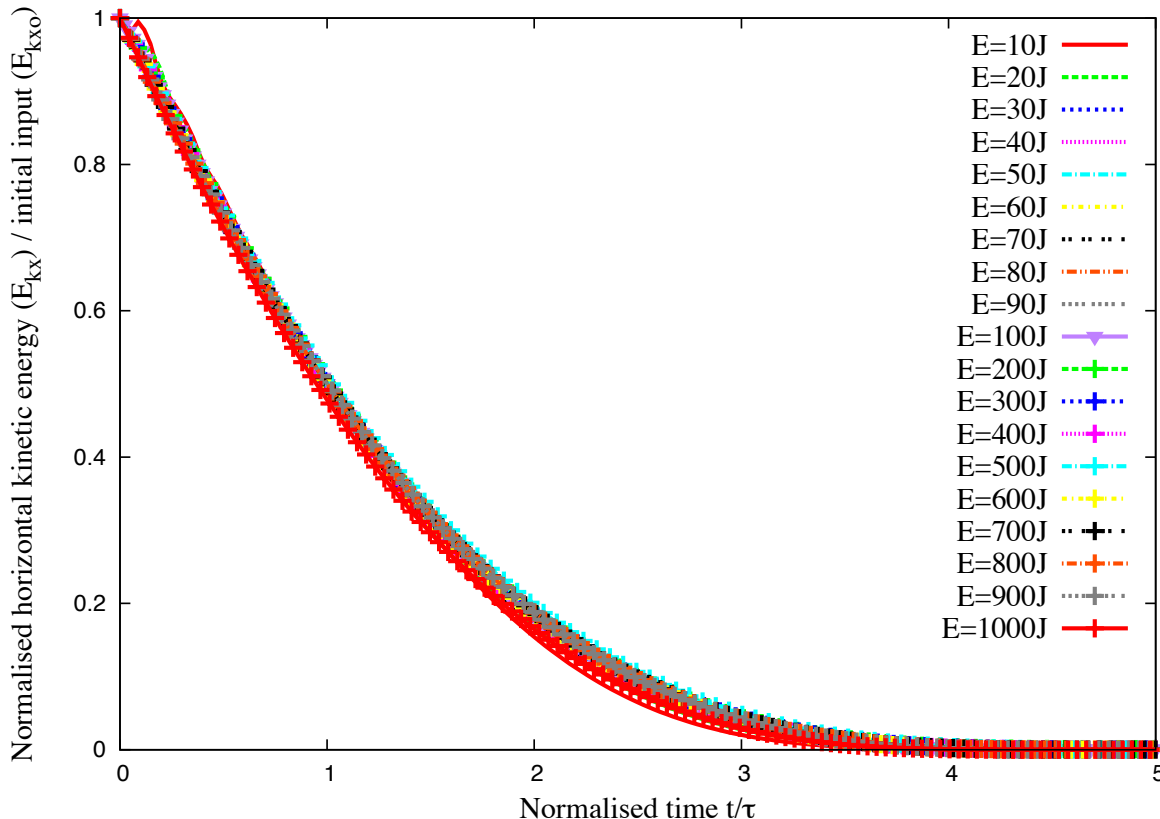


Figure 4.22 Evolution of kinetic energy in the x component of the velocity field normalized by the available kinetic energy at the end of the transient as a function of normalized time.

The scaling of the data with the decay time τ suggests also that the run-out time t'_f since the beginning of the second phase might be a simple function of τ . Figure 4.22 shows both t'_f and τ as a function of E'_{x0} , where we observe a power law for both times over nearly one decade. The run-out time $t'_f \propto (E'_{x0})^{\beta'}$ has the same exponent $\beta' \simeq 0.21 \pm 0.03$ as t_f as a function of E_0 (see Fig. 4.4). For the decay time we have $\tau \propto (E'_{x0})^{\beta''}$ with $\beta'' \simeq 0.28 \pm 0.03$. The relation

¹ between the two times can thus be expressed as

$$\text{2} \quad t'_f = k \tau (E'_{x0})^{\beta'' - \beta'}, \quad (4.11)$$

³ where $k \simeq 5 \pm 0.4$ and $\beta'' - \beta' \simeq -0.05 \pm 0.06$. This value is small enough to be neglected
⁴ within the confidence interval of our data. It is therefore plausible to assume that the run-out
⁵ time is a multiple of the decay time and the spreading process is controlled by a single time.
⁶ We however note that a weak dependence on the energy E'_{x0} is consistent with the fact that the
⁷ whole available energy at the beginning of the second phase is not dissipated in the spreading
⁸ process (calculated from the position of the tip of the pile) since the pile keeps deforming by
⁹ the movements of the particles at the free surface even when the tip comes to rest. This can
¹⁰ explain the small difference between the two exponents as observed here.

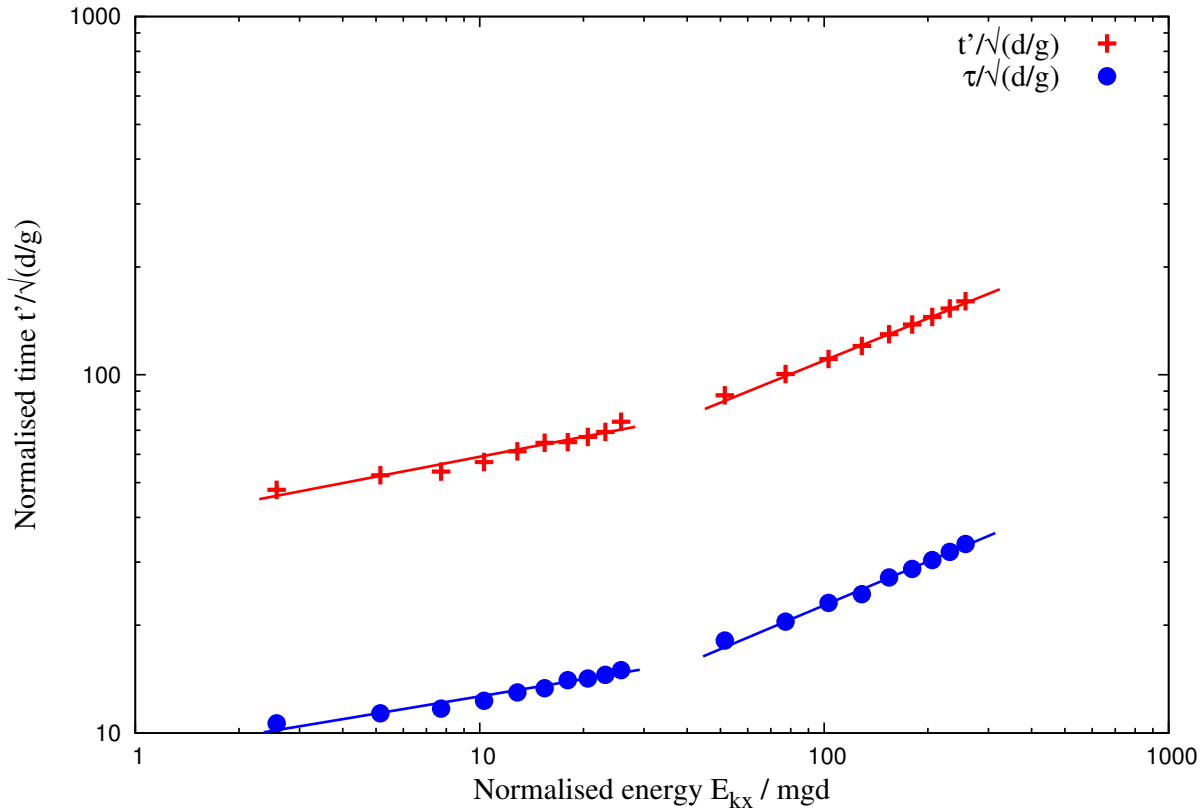


Figure 4.23 Power law evolution of t'_f and τ as a function of kinetic energy E_{kx0} .

¹¹ 4.3.4 Effect of friction

¹² The run-out distance and time and the dissipation of kinetic energy are controlled by the input
¹³ energy and collective dynamics of the whole pile, as it was analyzed in the previous sections.

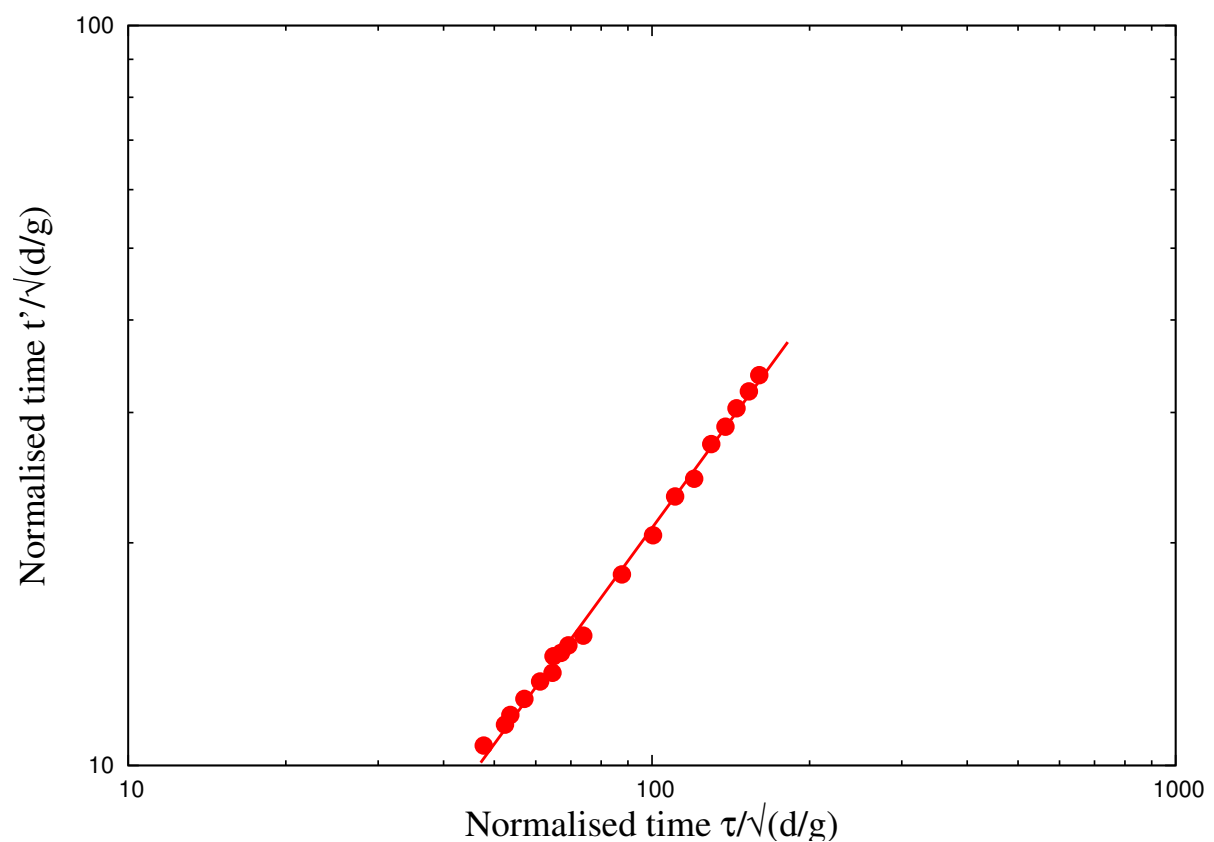


Figure 4.24 Linear relationship between decay time and run-out time after the transient as a function of the normalised kinetic energy E_{kx0} .

1 But they are expected to depend also on the friction. We performed a series of simulations with
 2 different values of base friction. The results are shown in Fig. ?? for the profiles of the pile and
 3 evolution of the kinetic energy in time. We see no difference in the results for different values
 4 of $e_n = e_t$. This is a consequence of the fact that, even at large input energies, the pile remains
 5 in a dense state so that multiple collisions inside the pile occur at small time scales compared
 6 to the deformation time. When the restitution coefficients are increased, more collisions occur
 7 during a longer time interval but the overall energy dissipation rate by collisions remains the
 8 same. This effect is a seminal example of collective effects which erase the influence of local
 9 parameters at the macroscopic scale. In contrast with the restitution coefficients, however, the
 10 effect of the friction coefficient is quite important for the run-out, as observed in Fig. ?? for
 11 both the energy decay and geometrical profile of the pile. Both the run-out distance and decay
 12 time decrease as the friction coefficient is increased. This effect is much more pronounced at
 13 low values of the friction coefficient. The run-out time, for example, is reduced by a factor 4 as
 14 μ_s is increased from 0.1 to 0.4 while the run-out times and profiles do not change much for
 15 $\mu_s = 0.7$. This “saturation effect” was evidenced in a systematic way in simple shear tests and
 16 explained by the observation that the dissipation rate may reach a saturation point where the
 17 dilation of the granular material and rolling of the particles change in response to the increase
 18 of the friction coefficient [Estrada et al. \(2008\)](#).

19

20 Mode of dissipation

21 The choice of this geometry was motivated by our main goal to focus on the effect of an input
 22 energy on the consecutive dynamics of a granular material. For the range of input energies
 23 investigated in this pushing test by means of contact dynamics simulations, we observed a
 24 power-law dependence of the run-out distance and time with non-trivial exponents. This is
 25 a central result of this work as it reveals that the power-law behaviour is a generic feature of
 26 granular dynamics. The values of the exponents are not simple functions of the geometry.

27 We also evidenced two regimes with different values of the exponents: a low-energy
 28 regime and a high-energy regime. The first regime reflects mainly the destabilization of the
 29 pile by the quake with a run-out time independent of the input energy whereas the second
 30 regime is governed by the spreading dynamics induced by the higher value of the input energy.
 31 We showed that the evolution of the pile in this high-energy regime can be described by a
 32 characteristic decay time and the energy available at the end of the first stage where the pile is
 33 destabilized by the quake.

34 This work may be pursued along two directions: 1) experimental realization of a similar
 35 setup with different modes of energy injection and 2) investigating the effect of various particle

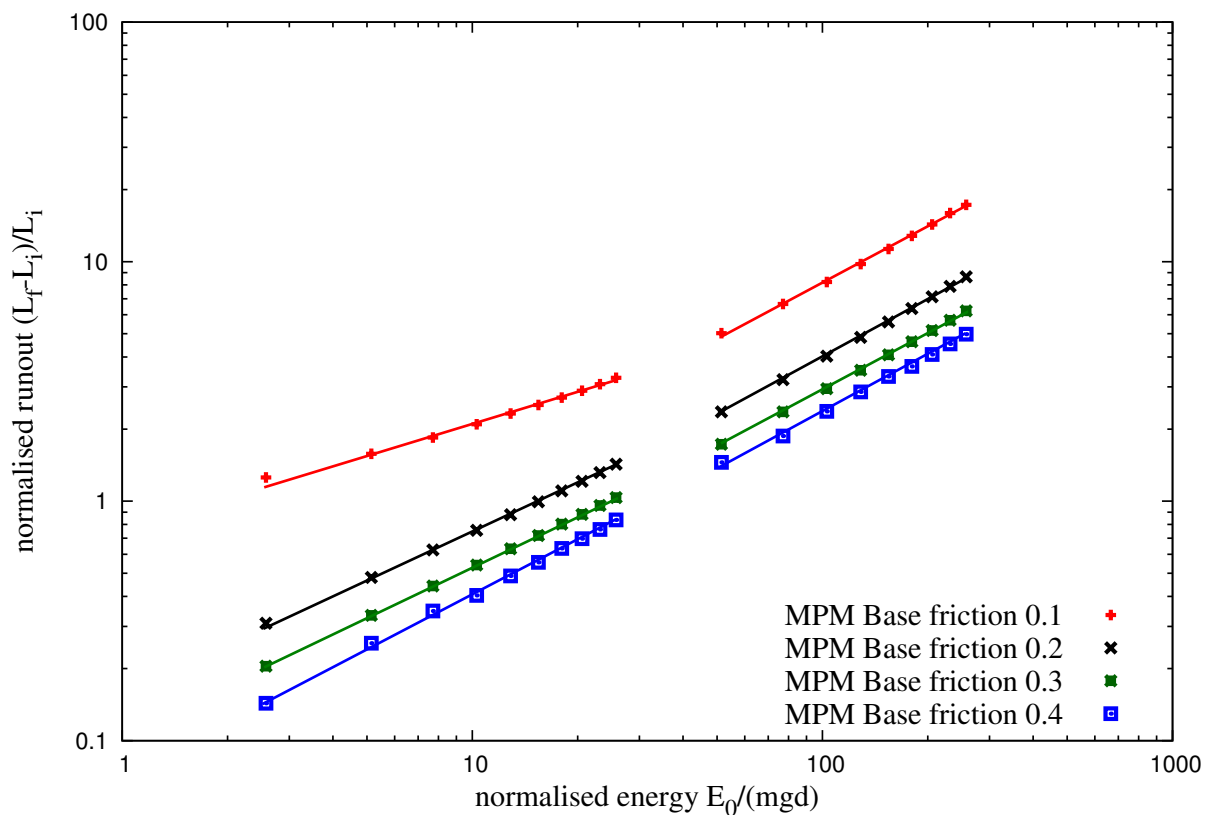


Figure 4.25 Effect of friction on the run-out distance as a function of the normalised input kinetic energy E_0 .

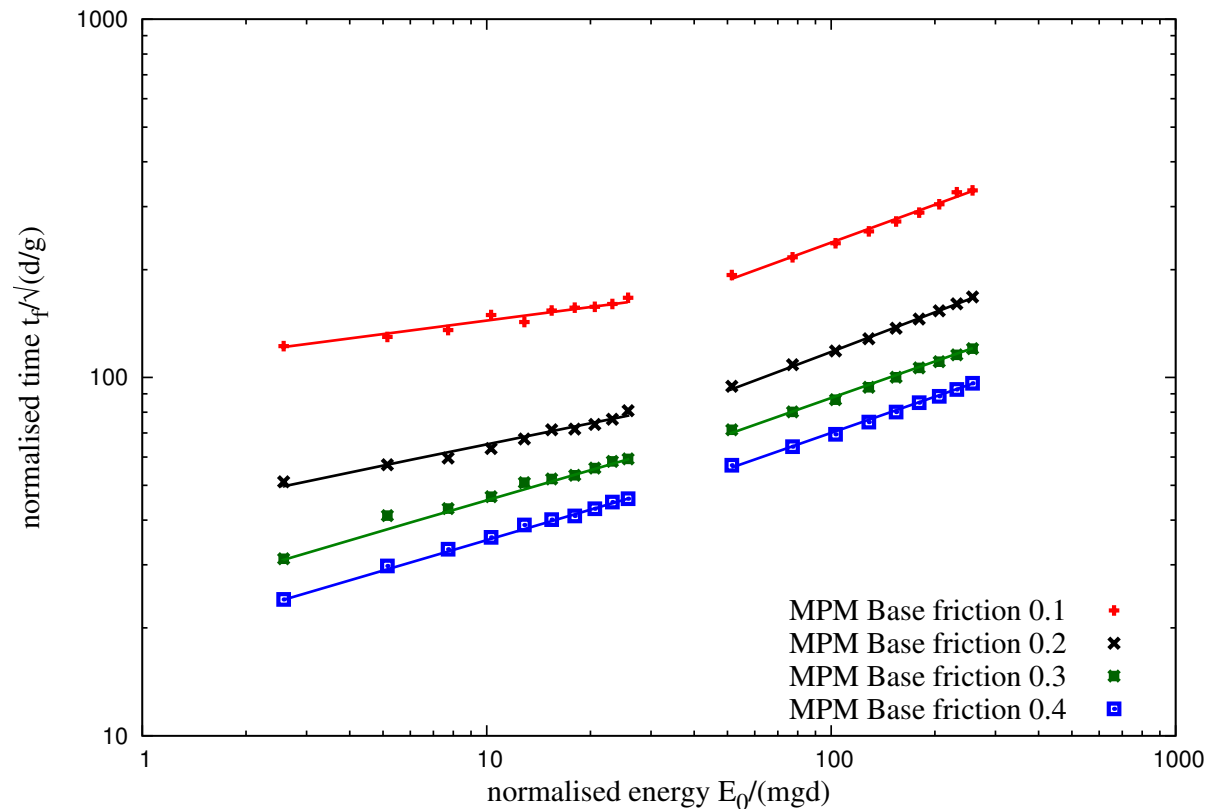


Figure 4.26 Effect of friction on the duration of run-out as a function of the normalised input kinetic energy E_0 .

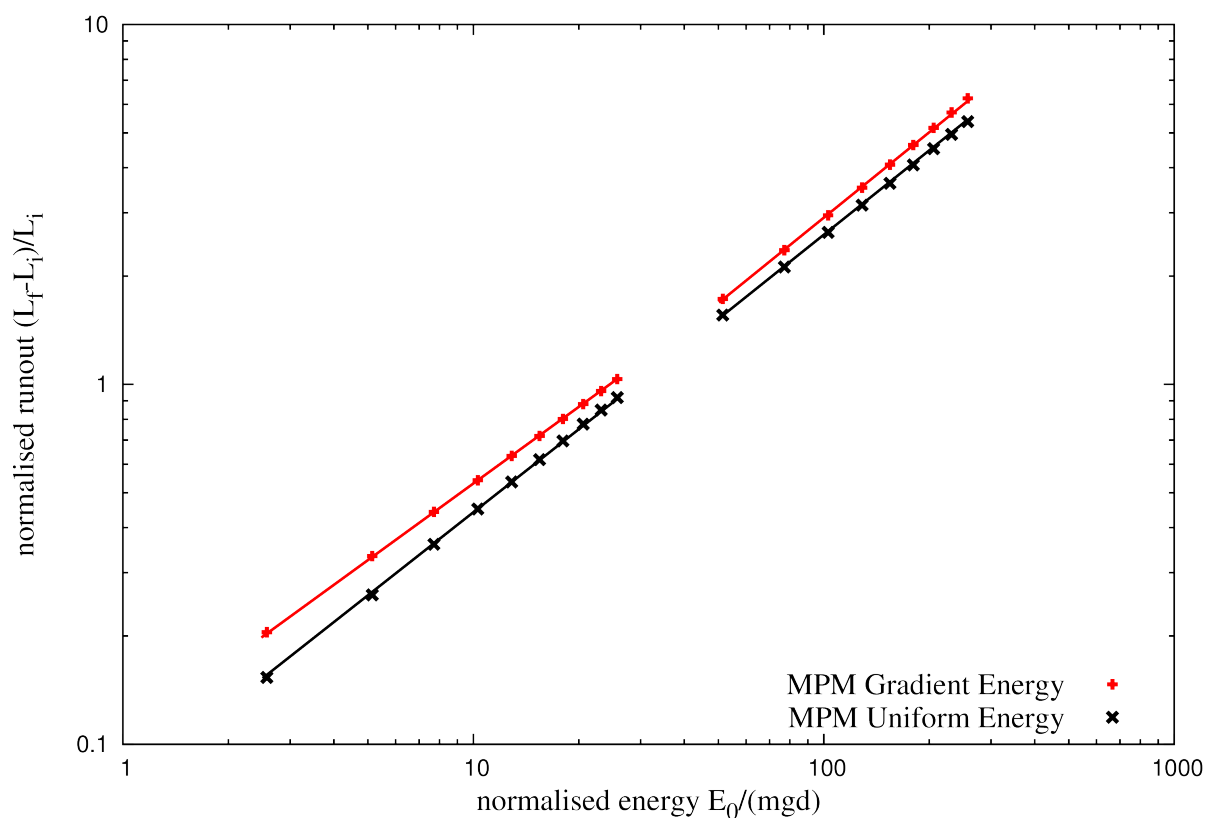


Figure 4.27 Effect of input velocity distribution on the run-out distance with normalised input kinetic energy

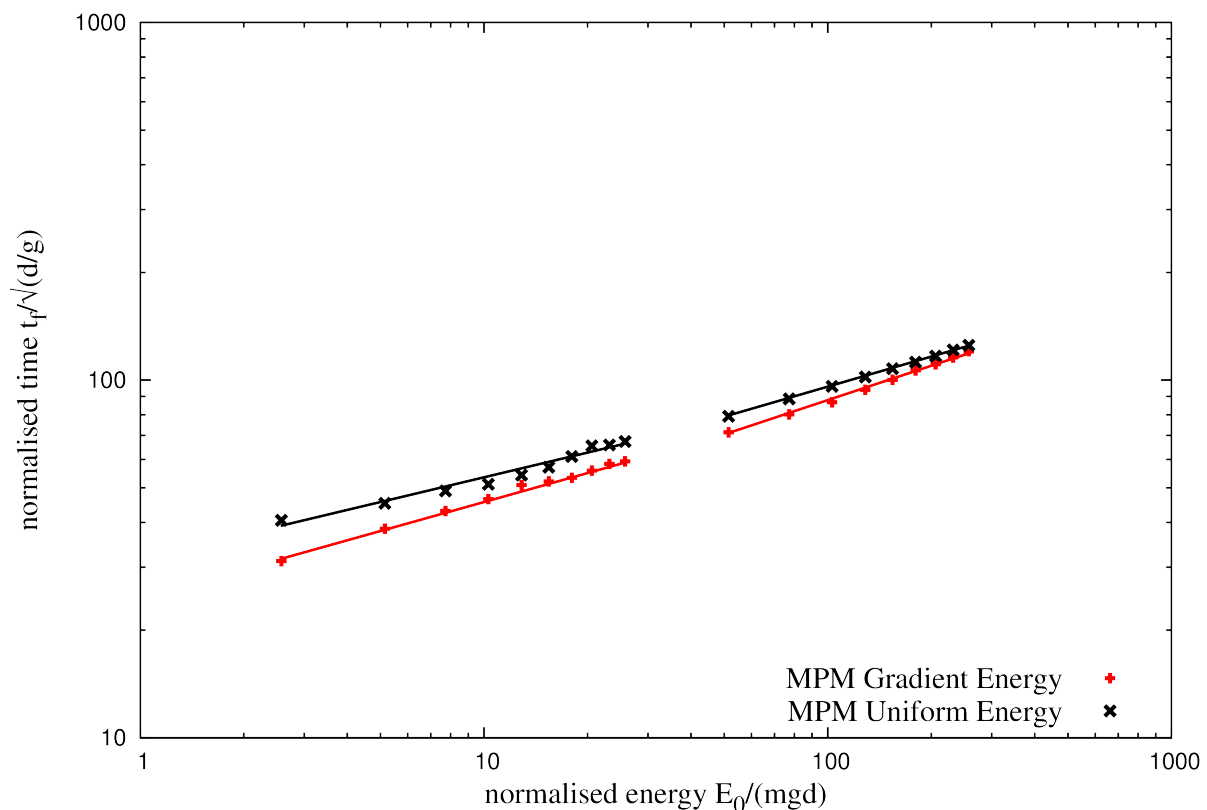


Figure 4.28 Effect of input velocity distribution on the duration of run-out with normalised input kinetic energy

shapes or the presence of an ambient fluid. Although numerical simulations are generally reliable with realistic results found in the past studies of steady flows, we believe that the transients are more sensitive situations than steady states and the experiments are necessary for checking the validation of the results suggested by the simulations. Provided a convenient method is used for supplying kinetic energy homogeneously into a pile, our configuration is also interesting for the investigation of the behavior of a pile immersed in a viscous fluid.

4.3.5 Effect of material points

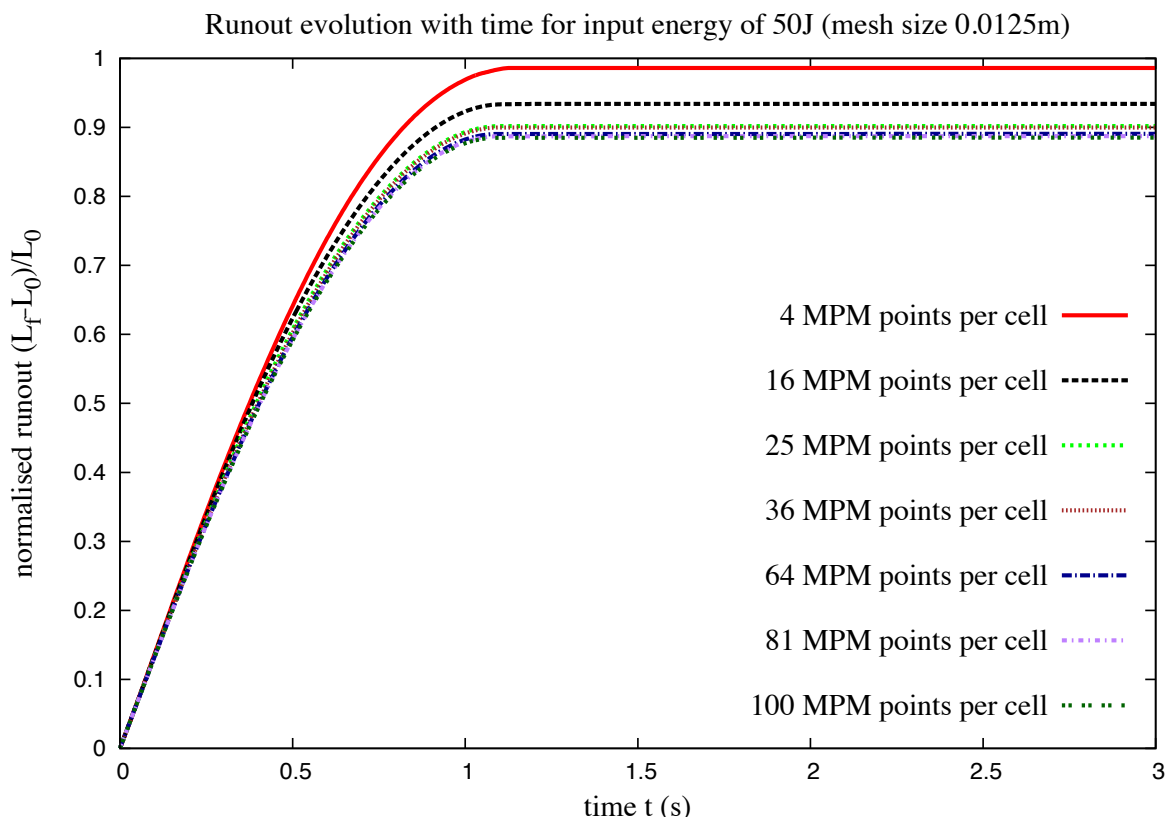


Figure 4.29 Evolution of run-out with time for varying material points per cell ($E_0 = 12.7mgd$).

4.3.6 Comparison with granular column collapse

4.4 Summary

Multi-scale simulation of granular column collapse was performed to understand the ability and limitations of continuum models to capture the micro-mechanics of dense granular flows. The

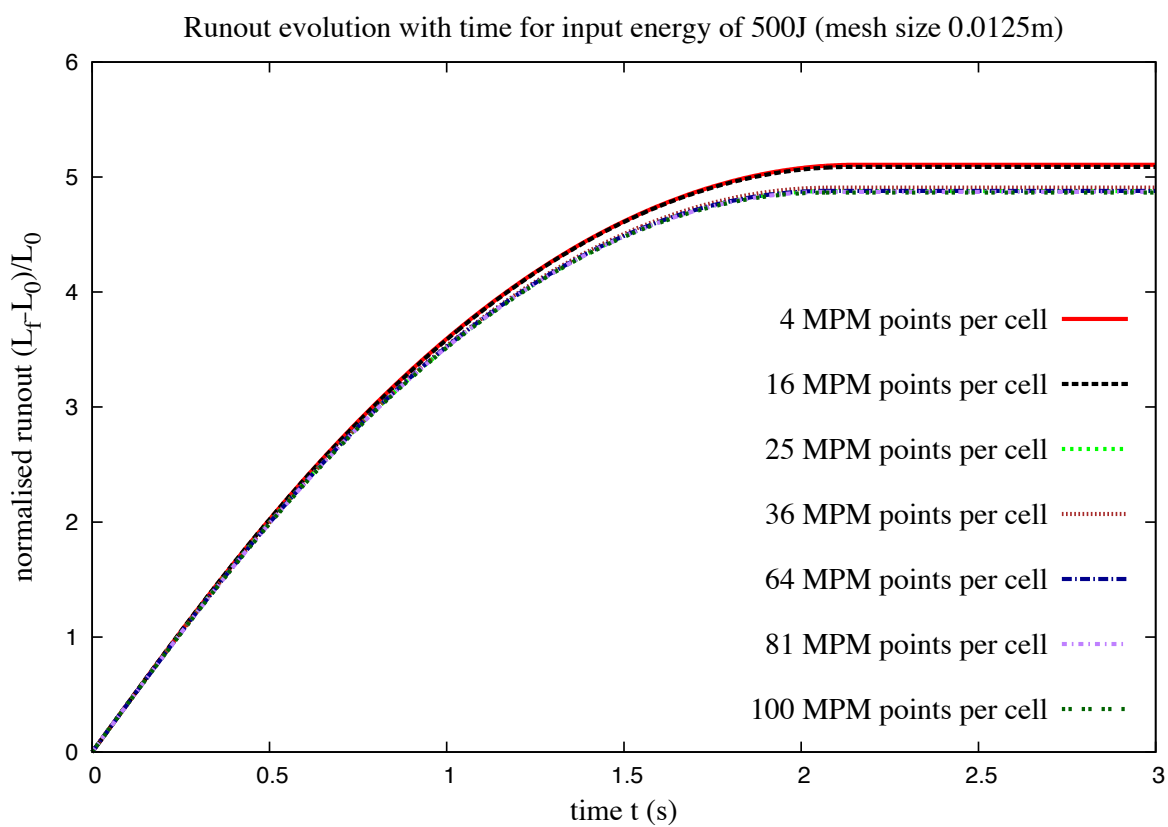


Figure 4.30 Evolution of run-out with time for varying material points per cell ($E_0 = 152mgd$).

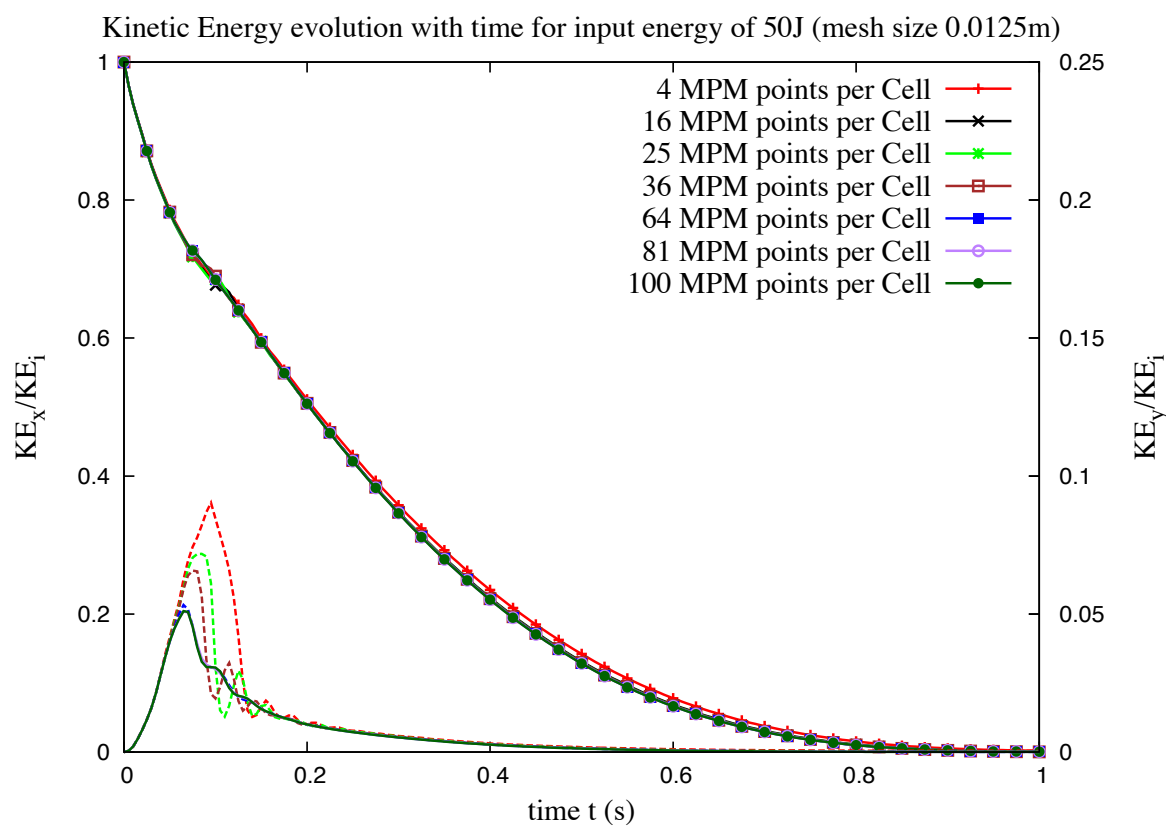


Figure 4.31 Evolution of kinetic energy with time for varying material points per cell ($E_0 = 12.7mgd$).

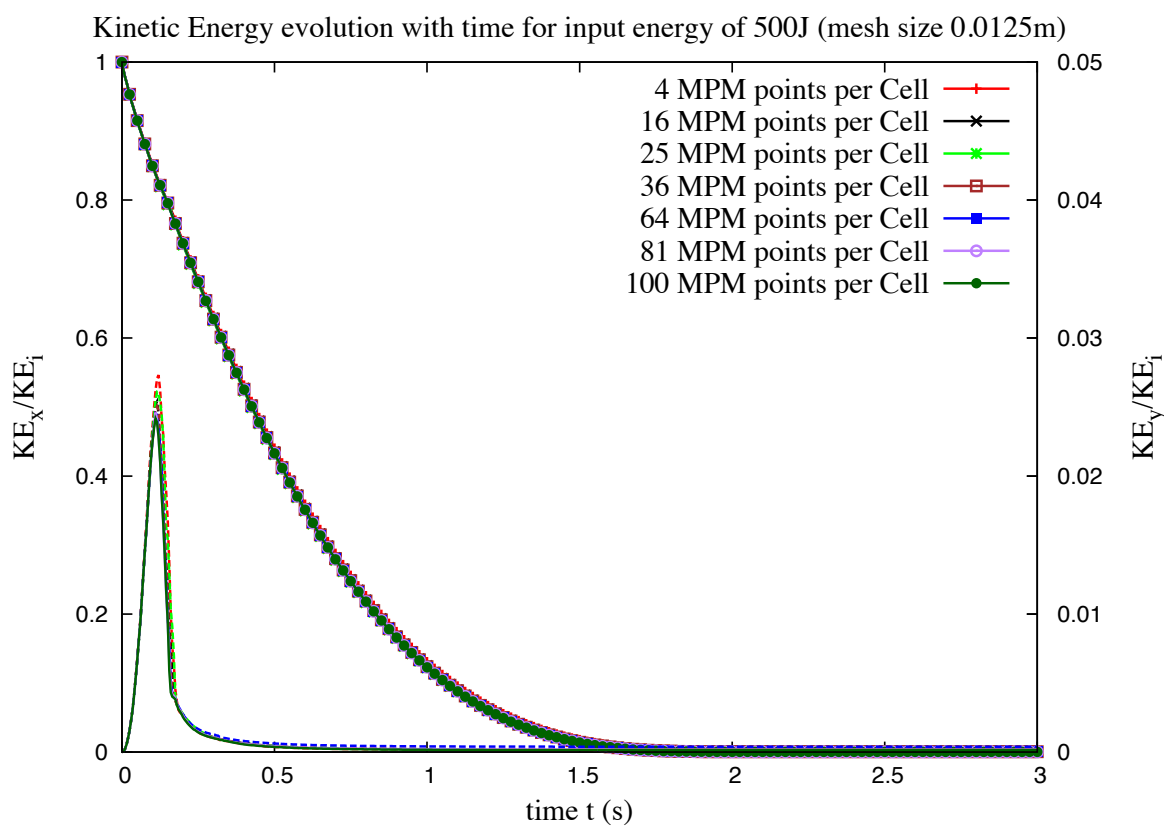


Figure 4.32 Evolution of kinetic with time for varying material points per cell ($E_0 = 152mgd$).

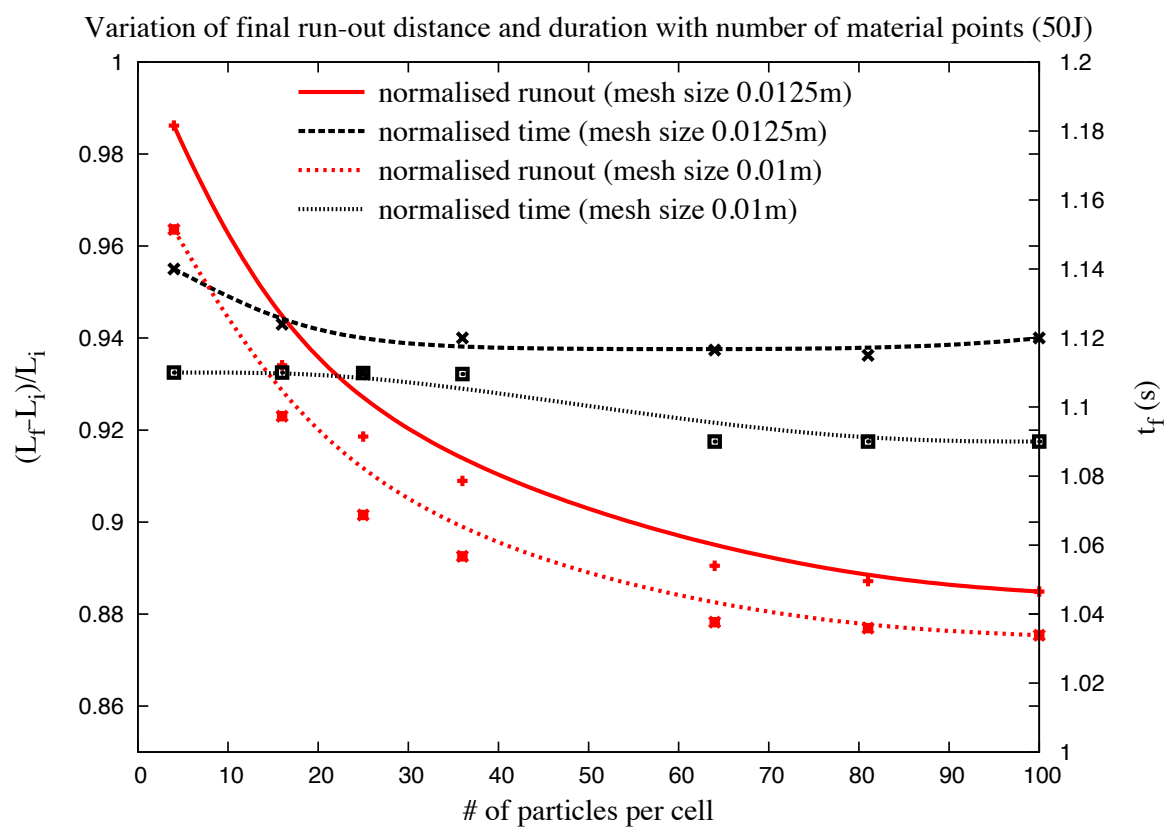


Figure 4.33 Evolution of run-out and duration of flow for varying material points per cell ($E_0 = 12.7mgd$).

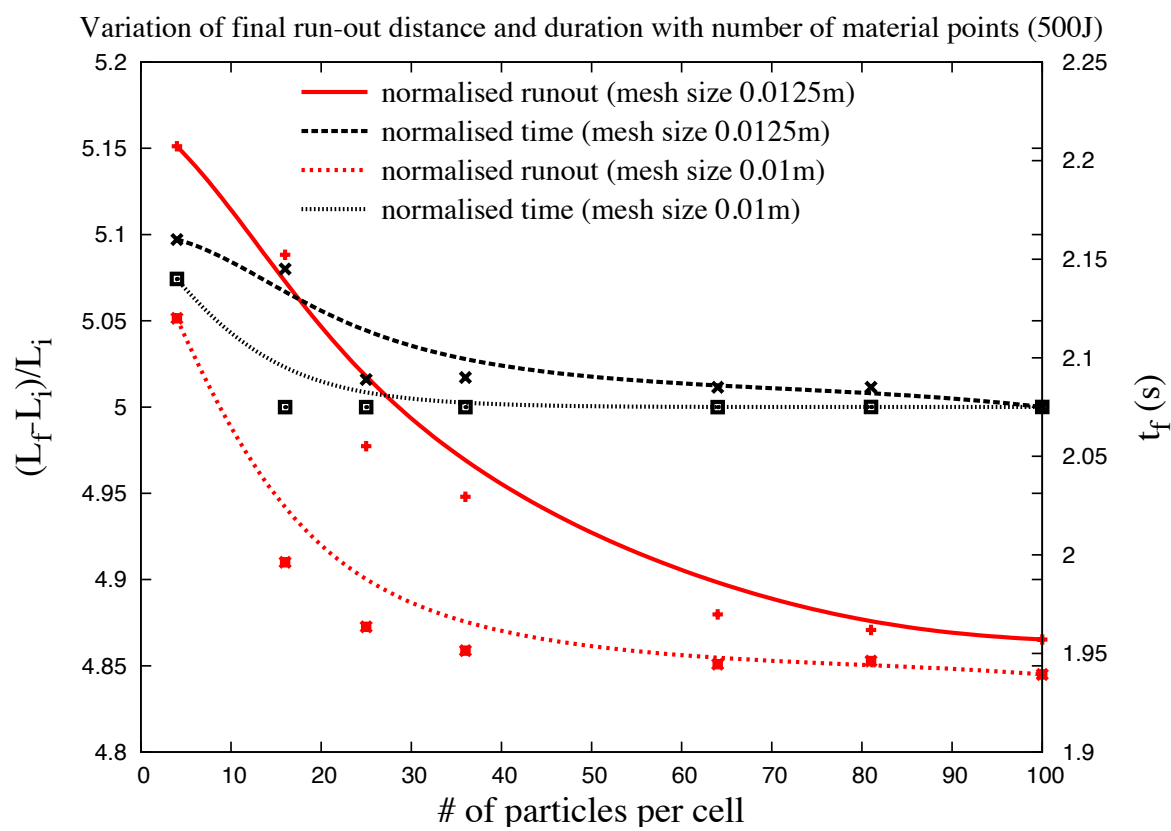


Figure 4.34 Evolution of run-out and duration of flow for varying material points per cell ($E_0 = 152mgd$).

run-out behaviour predicted by both continuum and DEM simulations matches for columns with small aspect ratios, where the dissipation is predominantly frictional. However, MPM predicts larger run-out distances for columns with higher aspect ratios. Energy evolution studies using DEM simulations reveal that the run-out behaviour is independent of frictional properties of the granular material and collision predominates the initial free-fall regime. The lack of a collisional energy dissipation mechanism in MPM results in over prediction of run-out distances.

1
2
3
4
5
6
7

Draft - v1.0

Saturday 13th September, 2014 – 10:18

References

- Balmforth, N. J. and Kerswell, R. R. (2005). Granular collapse in two dimensions. *Journal of Fluid Mechanics*, 538:399–428. 1
2
3
- Bandara, S. (2013). *Material Point Method to simulate Large Deformation Problems in Fluid-saturated Granular Medium*. PhD thesis, University of Cambridge. 4
5
- Daerr, A. and Douady, S. (1999). Two types of avalanche behaviour in granular media. *Nature*, 399(6733):241–243. 6
7
- Estrada, N., Taboada, A., and Radjai, F. (2008). Shear strength and force transmission in granular media with rolling resistance. *Physical Review E*, 78(2):021301. 8
9
- Guilkey, J., Harman, T., Xia, A., Kashiwa, B., and McMurtry, P. (2003). An Eulerian-Lagrangian approach for large deformation fluid structure interaction problems, Part 1: algorithm development. *Advances in Fluid Mechanics*, 36:143–156. 10
11
12
- Jean, M. (1999). The non-smooth contact dynamics method. *Computer Methods in Applied Mechanics and Engineering*, 177(3-4):235–257. 13
14
- Lacaze, L. and Kerswell, R. R. (2009). Axisymmetric Granular Collapse: A Transient 3D Flow Test of Viscoplasticity. *Physical Review Letters*, 102(10):108305. 15
16
- Lajeunesse, E., Mangeney-Castelnau, A., and Vilotte, J. P. (2004). Spreading of a granular mass on a horizontal plane. *Physics of Fluids*, 16(7):2371. 17
18
- Lube, G., Huppert, H. E., Sparks, R. S. J., and Freundt, A. (2005). Collapses of two-dimensional granular columns. *Physical Review E - Statistical, Nonlinear, and Soft Matter Physics*, 72(4):1–10. 19
20
21
- Moreau, J. J. (1993). New computation methods in granular dynamics. In *Powders & Grains 93*, page 227, Rotterdam. A. A. Balkema. 22
23
- Oda, M. and Iwashita, K. (1999). *Mechanics of granular materials: an introduction*. Taylor & Francis. 24
25
- Radjai, F. and Dubois, F. (2011). *Discrete-element modeling of granular materials*. ISTE Wiley, London; Hoboken, N.J. 26
27
- Radjai, F. and Richet, V. (2009). Contact dynamics as a nonsmooth discrete element method. *Mechanics of Materials*, 41(6):715–728. 28
29

- ¹ Schaefer, D. G. (1990). Instability and ill-posedness in the deformation of granular materials.
² *International Journal for Numerical and Analytical Methods in Geomechanics*, 14(4):253–
³ 278.
- ⁴ Staron, L., Radjai, F., and Vilotte, J. P. (2005). Multi-scale analysis of the stress state in
⁵ a granular slope in transition to failure. *The European physical journal. E, Soft matter*,
⁶ 18(3):311–20.
- ⁷ Topin, V., Monerie, Y., Perales, F., and Radjaï, F. (2012). Collapse Dynamics and Runout of
⁸ Dense Granular Materials in a Fluid. *Physical Review Letters*, 109(18):188001.